Sensitivity projections for a dual-phase argon TPC optimized for light dark matter searches through the ionization channel

Preprint · September 2022

CITATIONS
0

READS
270

299 authors, including:

Paolo Agnes
AstroParticle and Cosmology Laboratory
71 PUBLICATIONS **3,055** CITATIONS
SEE PROFILE

Sebastiano Albergo
University of Catania
252 PUBLICATIONS **8,256** CITATIONS
SEE PROFILE

Trenton Alexander
University of South Carolina
92 PUBLICATIONS **3,638** CITATIONS
SEE PROFILE

Pierre-André Amaudruz
TRIUMF
146 PUBLICATIONS **4,155** CITATIONS
SEE PROFILE

Sensitivity projections for a dual-phase argon TPC optimized for light dark matter searches through the ionization channel

P. Agnes,[1,2] I. Ahmad,[3] S. Albergo,[4,5] I. F. M. Albuquerque,[6] T. Alexander,[7] A. K. Alton,[8] P. Amaudruz,[2] M. Atzori Corona,[9,10] D. J. Auty,[11] M. Ave,[6] I. Ch. Avetisov,[12] R. I. Avetisov,[12] O. Azzolini,[13] H. O. Back,[7] Z. Balmforth,[1] V. Barbarian,[14] A. Barrado Olmedo,[15] P. Barrillon,[16] A. Basco,[17] G. Batignani,[18,19] E. Berzin,[20] A. Bondar,[21,22] W. M. Bonivento,[10] E. Borisova,[21,22] B. Bottino,[23,24] M. G. Boulay,[25] G. Buccino,[26] S. Bussino,[27,28] J. Busto,[16] A. Buzulutskov,[21,22] M. Cadeddu,[10] M. Cadoni,[9,10] A. Caminata,[24] N. Canci,[17] A. Capra,[2] S. Caprioli,[24] M. Caravati,[10] M. Cárdenas-Montes,[15] N. Cargioli,[9,10] M. Carlini,[26] P. Castello,[29,10] V. Cataudella,[30,17] P. Cavalcante,[26] S. Cavuoti,[30,17,31] S. Cebrian,[32] J. M. Cela Ruiz,[15] S. Chashin,[14] A. Chepurnov,[14] E Chyhyrynets,[13] C. Cicalò,[10] L. Cifarelli,[33,34] D. Cintas,[32] V. Cocco,[10] E. Conde Vilda,[15] L. Consiglio,[26] S. Copello,[24,23] G. Covone,[30,17] S. Cross,[35] P. Czudak,[36] M. D'Aniello,[37] S. D'Auria,[38] M. D. Da Rocha Rolo,[39] O. Dadoun,[40] M. Daniel,[15] S. Davini,[24] A. De Candia,[30,17] S. De Cecco,[41,42] A. De Falco,[9,10] G. De Filippis,[30,17] D. De Gruttola,[43,44] S. De Pasquale,[43,44] G. De Rosa,[30,17] G. Dellacasa,[39] A. V. Derbin,[45] A. Devoto,[9,10] F. Di Capua,[30,17] L. Di Noto,[24] P. Di Stefano,[46] C. Dionisi,[41,42] G. Dolganov,[47] F. Dordei,[10] L. Doria,[48] T. Erjavec,[49] M. Fernandez Diaz,[15] G. Fiorillo,[30,17] A. Franceschi,[50] P. Franchini,[51,1] D. Franco,[52] E. Frolov,[21,22] N. Funicello,[43,44] F. Gabriele,[10] D. Gahan,[9,10] C. Galbiati,[20,26,53] G. Gallina,[20] G. Gallus,[10,29] M. Garbini,[54,34] P. Garcia Abia,[15] A. Gendotti,[55] C. Ghiano,[26] R. A. Giampaolo,[39,53] C. Giganti,[40] M. A. Giorgi,[19,18] G. K. Giovanetti,[56] V. Goicoechea Casanueva,[57] A. Gola,[58,59] D. Gorman,[35] R. Graciani Diaz,[60] G. Grauso,[17] G. Grilli di Cortona,[50] A. Grobov,[47,61] M. Gromov,[14,62] M. Guan,[63] M. Guerzoni,[34] M. Gulino,[64,65] C. Guo,[63] B. R. Hackett,[7] J. B. Hall,[20] A. L. Hallin,[11] A. Hamer,[66,1] H. Helton,[20] M. Haranczyk,[36] T. Hessel,[52] S. Hill,[1] S. Horikawa,[67,26] F. Hubaut,[16] T. Hugues,[3] E. V. Hungerford,[68] An. Ianni,[20,26] V. Ippolito,[41] C. Jillings,[69,70] P. Kachru,[53,26] A. A. Kemp,[46] C. L. Kendziora,[71] G. Keppel,[13] A. V. Khomyakov,[12] M. Kimura,[3] I. Kochanek,[26] K. Kondo,[26] G. Korga,[1] S. Koulosousas,[1] A. Kubankin,[72] M. Kuss,[18] M. Kuźniak,[3] M. La Commara,[73,17] M. Lai,[9,10] E. Le Guirriec,[16] E. Leason,[1] X. Li,[20] L. Lidey,[7] J. Lipp,[35] M. Lissia,[10] G. Longo,[30,17] L. Luzzi,[15] O. Macfadyen,[1] I. N. Machulin,[47,61] I. Manthos,[74] L. Mapelli,[20] A. Margotti,[34] S. M. Mari,[27,28] C. Mariani,[75] J. Maricic,[57] A. Marini,[23,24] M. Martínez,[32,76] C. J. Martoff,[77] A. Masoni,[10] K. Mavrokoridis,[78] A. Mazzi,[58,59] A. B. McDonald,[46] A. Messina,[41,42] R. Milincic,[57] A. Moggi,[18] A. Moharana,[53,26] J. Monroe,[1] M. Morrocchi,[18,19] E. N. Mozhevitina,[12] T. Mróz,[36] V. N. Muratova,[45] C. Muscas,[29,10] P. Musico,[24] R. Nania,[34] T. Napolitano,[50] M. Nessi,[79] G. Nieradka,[3] K. Nikolopoulos,[74] I. Nikulin,[72] J. Nowak,[51] K. Olchansky,[2] A. Oleinik,[72] V. Oleynikov,[21,22] P. Organtini,[20,26] A. Ortiz de Solórzano,[32] L. Pagani,[49] M. Pallavicini,[23,24] L. Pandola,[65] E. Pantic,[49] E. Paoloni,[18,19] G. Paternoster,[58,59] P. A. Pegoraro,[29,10] K. Pelczar,[36] C. Pellegrino,[34] F. Perotti,[80,38] V. Pesudo,[15] S. Piacentini,[42,41] F. Pietropaolo,[79] N. Pino,[4,5] C. Pira,[13] A. Pocar,[81] D. M. Poehlmann,[49] S. Pordes,[71] P. Pralavorio,[16] D. Price,[82] F. Raffaelli,[18] F. Ragusa,[83,38] Y. Ramachers,[84] A. Ramirez,[68] M. Razeti,[10] A. Razeto,[26] A. L. Renshaw,[68] M. Rescigno,[41] F. Resnati,[79] F. Retiere,[2] L. P. Rignanese,[34,33] C. Ripoli,[44,43] A. Rivetti,[39] A. Roberts,[78] C. Roberts,[78] J. Rode,[40,52] G. Rogers,[74] L. Romero,[15] M. Rossi,[24,23] A. Rubbia,[55] S. Sadashivajois,[1] T. R. Saffold,[56] O. Samoylov,[62] E. Sandford,[82] S. Sanfilippo,[65] D. Santone,[1] R. Santorelli,[15] C. Savarese,[20] E. Scapparone,[34] G. Scioli,[33,34] D. A. Semenov,[45] A. Shchagin,[72] A. Sheshukov,[62] M. Simeone,[85,17] P. Skensved,[46] M. D. Skorokhvatov,[47,61] O. Smirnov,[62] T. Smirnova,[47] B. Smith,[2] A. Sokolov,[21,22] M. Spangenberg,[84] R. Stefanizzi,[9,10] A. Steri,[10] S. Stracka,[18] V. Strickland,[25] M. Stringer,[46] S. Sulis,[29,10] A. Sung,[20] Y. Suvorov,[30,17,47] A. M. Szelc,[66] C. Türkoğlu,[3] R. Tartaglia,[26] A. Taylor,[78] J. Taylor,[78] S. Tedesco,[39,86] G. Testera,[24] K. Thieme,[57] T. N. Thorpe,[87] A. Tonazzo,[52] S. Torres-Lara,[68] A. Tricomi,[4,5] E. V. Unzhakov,[45] T. Vallivilayil John,[53,26] M. Van Uffelen,[16] T. Viant,[55] S. Viel,[25] A. Vishneva,[62] R. B. Vogelaar,[75] J. Vossebeld,[78] M. Wada,[3,9] M. B. Walczak,[3] Y. Wang,[63,88] S. Westerdale,[89,20] R. J. Wheadon,[39] L. Williams,[90] I. Wingerter-Seez,[16] R. Wojaczyński,[3] Ma. M. Wojcik,[36] Ma. Wojcik,[91] T. Wright,[75] Y. Xie,[63,88] C. Yang,[63,88] A. Zabihi,[3] P. Zakhary,[3] A. Zani,[38] A. Zichichi,[33,34] G. Zuzel,[36] and M. P. Zykova[12]

(Global Argon Dark Matter Collaboration)*

[1]*Department of Physics, Royal Holloway University of London, Egham TW20 0EX, UK*
[2]*TRIUMF, 4004 Wesbrook Mall, Vancouver, BC V6T 2A3, Canada*
[3]*AstroCeNT, Nicolaus Copernicus Astronomical Center of the Polish Academy of Sciences, 00-614 Warsaw, Poland*
[4]*INFN Catania, Catania 95121, Italy*
[5]*Università of Catania, Catania 95124, Italy*
[6]*Instituto de Física, Universidade de São Paulo, São Paulo 05508-090, Brazil*
[7]*Pacific Northwest National Laboratory, Richland, WA 99352, USA*
[8]*Physics Department, Augustana University, Sioux Falls, SD 57197, USA*
[9]*Physics Department, Università degli Studi di Cagliari, Cagliari 09042, Italy*
[10]*INFN Cagliari, Cagliari 09042, Italy*
[11]*Department of Physics, University of Alberta, Edmonton, AB T6G 2R3, Canada*
[12]*Mendeleev University of Chemical Technology, Moscow 125047, Russia*
[13]*INFN Laboratori Nazionali di Legnaro, Legnaro (Padova) 35020, Italy*
[14]*Skobeltsyn Institute of Nuclear Physics, Lomonosov Moscow State University, Moscow 119234, Russia*
[15]*CIEMAT, Centro de Investigaciones Energéticas, Medioambientales y Tecnológicas, Madrid 28040, Spain*
[16]*Centre de Physique des Particules de Marseille, Aix Marseille Univ, CNRS/IN2P3, CPPM, Marseille, France*
[17]*INFN Napoli, Napoli 80126, Italy*
[18]*INFN Pisa, Pisa 56127, Italy*
[19]*Physics Department, Università degli Studi di Pisa, Pisa 56127, Italy*
[20]*Physics Department, Princeton University, Princeton, NJ 08544, USA*
[21]*Budker Institute of Nuclear Physics, Novosibirsk 630090, Russia*
[22]*Novosibirsk State University, Novosibirsk 630090, Russia*
[23]*Physics Department, Università degli Studi di Genova, Genova 16146, Italy*
[24]*INFN Genova, Genova 16146, Italy*
[25]*Department of Physics, Carleton University, Ottawa, ON K1S 5B6, Canada*
[26]*INFN Laboratori Nazionali del Gran Sasso, Assergi (AQ) 67100, Italy*
[27]*INFN Roma Tre, Roma 00146, Italy*
[28]*Mathematics and Physics Department, Università degli Studi Roma Tre, Roma 00146, Italy*
[29]*Department of Electrical and Electronic Engineering, Università degli Studi di Cagliari, Cagliari 09123, Italy*
[30]*Physics Department, Università degli Studi "Federico II" di Napoli, Napoli 80126, Italy*
[31]*INAF Osservatorio Astronomico di Capodimonte, 80131 Napoli, Italy*
[32]*Centro de Astropartículas y Física de Altas Energías, Universidad de Zaragoza, Zaragoza 50009, Spain*
[33]*Department of Physics and Astronomy, Università degli Studi di Bologna, Bologna 40126, Italy*
[34]*INFN Bologna, Bologna 40126, Italy*
[35]*Science & Technology Facilities Council (STFC), Rutherford Appleton Laboratory, Technology, Harwell Oxford, Didcot OX11 0QX, UK*
[36]*M. Smoluchowski Institute of Physics, Jagiellonian University, 30-348 Krakow, Poland*
[37]*Department of Strutture per l'Ingegneria e l'Architettura, Università degli Studi "Federico II" di Napoli, Napoli 80131, Italy*
[38]*INFN Milano, Milano 20133, Italy*
[39]*INFN Torino, Torino 10125, Italy*
[40]*LPNHE, CNRS/IN2P3, Sorbonne Université, Université Paris Diderot, Paris 75252, France*
[41]*INFN Sezione di Roma, Roma 00185, Italy*
[42]*Physics Department, Sapienza Università di Roma, Roma 00185, Italy*
[43]*Physics Department, Università degli Studi di Salerno, Salerno 84084, Italy*
[44]*INFN Salerno, Salerno 84084, Italy*
[45]*Saint Petersburg Nuclear Physics Institute, Gatchina 188350, Russia*
[46]*Department of Physics, Engineering Physics and Astronomy, Queen's University, Kingston, ON K7L 3N6, Canada*
[47]*National Research Centre Kurchatov Institute, Moscow 123182, Russia*
[48]*Institut für Kernphysik, Johannes Gutenberg-Universität Mainz, D-55128 Mainz, Germany*
[49]*Department of Physics, University of California, Davis, CA 95616, USA*
[50]*INFN Laboratori Nazionali di Frascati, Frascati 00044, Italy*
[51]*Physics Department, Lancaster University, Lancaster LA1 4YB, UK*
[52]*APC, Université de Paris, CNRS, Astroparticule et Cosmologie, Paris F-75013, France*
[53]*Gran Sasso Science Institute, L'Aquila 67100, Italy*
[54]*Museo Storico della Fisica e Centro Studi e Ricerche Enrico Fermi, Roma 00184, Italy*
[55]*Institute for Particle Physics, ETH Zürich, Zürich 8093, Switzerland*
[56]*Williams College, Physics Department, Williamstown, MA 01267 USA*
[57]*Department of Physics and Astronomy, University of Hawai'i, Honolulu, HI 96822, USA*
[58]*Fondazione Bruno Kessler, Povo 38123, Italy*
[59]*Trento Institute for Fundamental Physics and Applications, Povo 38123, Italy*

[60] Universiatat de Barcelona, Barcelona E-08028, Catalonia, Spain
[61] National Research Nuclear University MEPhI, Moscow 115409, Russia
[62] Joint Institute for Nuclear Research, Dubna 141980, Russia
[63] Institute of High Energy Physics, Beijing 100049, China
[64] Engineering and Architecture Faculty, Università di Enna Kore, Enna 94100, Italy
[65] INFN Laboratori Nazionali del Sud, Catania 95123, Italy
[66] School of Physics and Astronomy, University of Edinburgh, Edinburgh EH9 3FD, UK
[67] Università degli Studi dell'Aquila, L'Aquila 67100, Italy
[68] Department of Physics, University of Houston, Houston, TX 77204, USA
[69] SNOLAB, Lively, ON P3Y 1N2, Canada
[70] Department of Physics and Astronomy, Laurentian University, Sudbury, ON P3E 2C6, Canada
[71] Fermi National Accelerator Laboratory, Batavia, IL 60510, USA
[72] Radiation Physics Laboratory, Belgorod National Research University, Belgorod 308007, Russia
[73] Pharmacy Department, Università degli Studi "Federico II" di Napoli, Napoli 80131, Italy
[74] School of Physics and Astronomy, University of Birmingham, Edgbaston, B15 2TT, Birmingham, UK
[75] Virginia Tech, Blacksburg, VA 24061, USA
[76] Fundación ARAID, Universidad de Zaragoza, Zaragoza 50009, Spain
[77] Physics Department, Temple University, Philadelphia, PA 19122, USA
[78] Department of Physics, University of Liverpool, The Oliver Lodge Laboratory, Liverpool L69 7ZE, UK
[79] CERN, European Organization for Nuclear Research 1211 Geneve 23, Switzerland, CERN
[80] Civil and Environmental Engineering Department, Politecnico di Milano, Milano 20133, Italy
[81] Amherst Center for Fundamental Interactions and Physics Department, University of Massachusetts, Amherst, MA 01003, USA
[82] Department of Physics and Astronomy, The University of Manchester, Manchester M13 9PL, UK
[83] Physics Department, Università degli Studi di Milano, Milano 20133, Italy
[84] University of Warwick, Department of Physics, Coventry CV47AL, UK
[85] Chemical, Materials, and Industrial Production Engineering Department, Università degli Studi "Federico II" di Napoli, Napoli 80126, Italy
[86] Department of Electronics and Communications, Politecnico di Torino, Torino 10129, Italy
[87] Physics and Astronomy Department, University of California, Los Angeles, CA 90095, USA
[88] University of Chinese Academy of Sciences, Beijing 100049, China
[89] Department of Physics and Astronomy, University of California, Riverside, CA 92507, USA
[90] Department of Physics and Engineering, Fort Lewis College, Durango, CO 81301, USA
[91] Institute of Applied Radiation Chemistry, Lodz University of Technology, 93-590 Lodz, Poland

(Dated: 2022-09-05)

Dark matter lighter than $10\,\mathrm{GeV}/c^2$ encompasses a promising range of candidates. A conceptual design for a new detector, DarkSide-LowMass, is presented, based on the DarkSide-50 detector and progress toward DarkSide-20k, optimized for a low-threshold electron-counting measurement. Sensitivity to light dark matter is explored for various potential energy thresholds and background rates. These studies show that DarkSide-LowMass can achieve sensitivity to light dark matter down to the solar neutrino floor for GeV-scale masses and significant sensitivity down to $10\,\mathrm{MeV}/c^2$ considering the Migdal effect or interactions with electrons. Requirements for optimizing the detector's sensitivity are explored, as are potential sensitivity gains from modeling and mitigating spurious electron backgrounds that may dominate the signal at the lowest energies.

I. Introduction

Astrophysical evidence indicates that dark matter (DM) constitutes 26 % of the universe's energy density [1]. Many experiments have tried to detect it directly, often focused on Weakly Interacting Massive Particles (WIMPs) with mass between $10\,\mathrm{GeV}/c^2$ and $10\,\mathrm{TeV}/c^2$ [2–8]. Planned experiments [9–11] will search for WIMPs with cross sections below which Coherent Elastic Neutrino-Nucleus Scattering (CEνNS) from atmospheric neutrinos may obscure DM signals, called the "neutrino fog" [12, 13].

Past experiments show that similar technology can perform dedicated light DM searches [14–19]. DarkSide-50 demonstrated that a dual-phase liquid argon time-projection chamber (LAr TPC) performing an electron-counting analysis—focused on electroluminescence signals from ionization electrons in a gas pocket, S2—is sensitive to DM with nuclear couplings for 1–$10\,\mathrm{GeV}/c^2$ masses [20, 21] and electronic couplings for 0.01–$1\,\mathrm{GeV}/c^2$ masses [22].

Interactions in LAr produce a comparable amount of scintillation and ionization. While photons are detected with ∼20 % efficiency and must overcome

* ds-ed@lngs.infn.it

noise, the near-perfect efficiency for extracting electrons from liquid to gaseous argon [23], the long drift lifetime (enabled by excellent purity achievable in LAr), and gas pocket amplification lets each ionization electron be detected. As a result, the electron-counting channel accesses energies near the work function, lower than those reached by scintillation.

Dual-phase LAr TPCs benefit from scalability due to LAr's low cost and high transparency to photons and electrons; their low temperature enables exceptional purity, as seen in DEAP-3600's low ^{222}Rn concentration [24] and DarkSide-50's long electron drift lifetime [25]. The relatively light nucleus also allows light DM to produce higher-energy recoils.

These properties enable dual-phase LAr TPCs to search for light DM into the solar neutrino fog. Maximizing sensitivity requires a dedicated detector optimized for electron-counting analyses by enhancing S2 and minimizing backgrounds that produce $<3\,\mathrm{keV}$ electron equivalent ($\mathrm{keV_{ee}}$) signals, as expected from light DM. DarkSide-LowMass aims to employ such a detector. This paper explores its potential sensitivity, considering 2 and $4\,e^-$ analysis thresholds and possible background levels and detector response models. A conceptual design is presented in Sec. II; Sec. III describes response models, and Sec. IV explores background scenarios. Finally, Sec. V projects sensitivity with these models, and Sec. VI discusses potential future improvements.

II. Conceptual detector design

Based on lessons from DarkSide-50 and progress toward DarkSide-20k [14, 15, 20–22, 25–29], a conceptual detector has been designed to optimize DarkSide-LowMass for low-threshold analyses.

A. Lessons from DarkSide-50

While DarkSide-50 was designed for a high-mass WIMP search using primary scintillation (S1) and electroluminescence (S2), its sensitivity to light DM elucidates how a dual-phase LAr TPC can be optimized for an electron-counting analysis. This channel lacks S1, thereby losing the capacity to reject electronic recoils (ERs) by pulse shape discrimination and to reconstruct interactions' vertical positions [30]. DarkSide-50's sensitivity was limited by ERs due to γ-rays from the photomultiplier tubes and cryostat and β-decays of trace residual ^{85}Kr and ^{39}Ar in the argon extracted from underground (UAr) [31, 32]. At the lowest energies, spurious electrons (SEs), not directly produced by energy depositions, dominate $<4\,e^-$ backgrounds, imposing an effective analysis threshold. Mitigating SEs is key to improving DarkSide-LowMass's sensitivity.

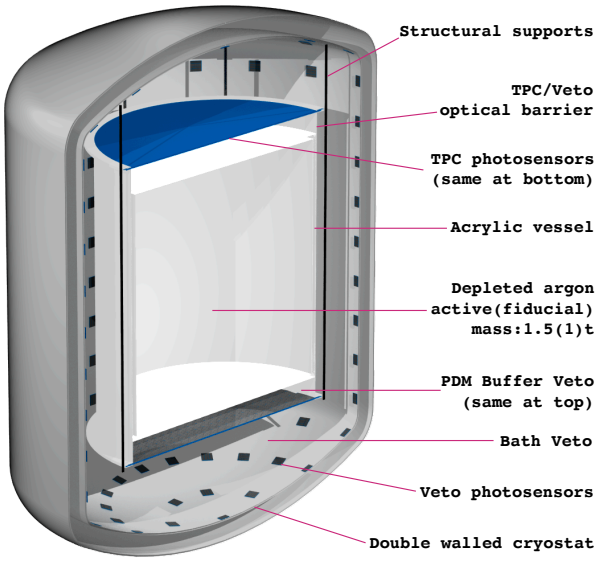

FIG. 1. Conceptual detector design: a 1.5 t dual-phase LAr TPC in an acrylic vessel, viewed by two photosensor arrays via 10 cm "buffer vetoes", in a UAr "bath veto" in a cryostat, immersed in a water tank (not shown).

B. Detector description

TABLE I. Conceptual detector design parameters.

Parameter	Value
TPC active LAr mass	1.5 t
TPC fiducial LAr mass	1 t
TPC fiducial cylindrical radius	45 cm
TPC height	111 cm
TPC diameter	110 cm
TPC PDM number	864
TPC PDM peak efficiency	40 %
TPC gas pocket thickness	1 cm
TPC electroluminescence field	6.5 kV/cm
TPC drift field	200 V/cm
Acrylic vessel mass	0.144 t
PDM dimensions	$5 \times 5\,\mathrm{cm}^2$
PDM buffer veto thickness	10 cm
PDM buffer veto total mass	0.3 t
Bath veto UAr mass	4.5 t
Bath veto minimum thickness	28 cm
Cryostat inner height	215 cm
Cryostat inner diameter	170 cm
Cryostat wall thickness	0.5 cm
Ti support structure total mass	0.1 t

Figure 1 shows a conceptual DarkSide-LowMass design; Table I gives design parameters. The nested structure isolates and vetoes against radioactivity. The detector consists of the following elements:

a. Depleted Argon TPC: the inner detector is a dual-phase TPC with an active (fiducial) mass of

1.5 t (1 t) of UAr, depleted of ^{39}Ar by cryogenic distillation [26]. The TPC has an ultra-pure acrylic vessel, as in DEAP-3600 [33]. Transparent conductive films like Clevios$^{\text{TM}}$ define anode and cathode planes; rings coated on the walls ensure spatial uniformity of the drift field. Electroluminescence in a 1 cm-thick gas pocket at the top allows extracted electrons to be counted. A stainless steel grid below the LAr surface separates the drift volume from the extraction and multiplication regions, with a 200 V/cm drift field in the bulk and a 6.5 kV/cm electroluminescence field in the gas pocket, building on experience from DarkSide-50. The expected extraction efficiency exceeds 99.9 % [23].

The vessel's inner surfaces are lined with reflector coated with wavelength shifter like TPB (tetraphenyl butadiene), which shifts VUV photons emitted by argon to ∼420 nm. Two planes of photodetector modules (PDMs) with 100% optical coverage, mounted 10 cm above and below the TPC, detect this light. Each PDM is a $5 \times 5\,\text{cm}^2$ array of silicon photomultipliers (SiPMs) based on Ref. [34], readout by cryogenic pre-amplifiers developed for DarkSide-20k [35]. Titanium structural supports hold the TPC and optical planes; titanium allows them to be radiopure and lightweight, reducing their impact on the vetoes and background budget. This system is immersed in a UAr bath held in a double-walled, 170 cm-diameter stainless steel cryostat.

For these studies, the TPC has equal diameter and height in order to maximize the path that external γ-rays must traverse before reaching the fiducial volume. This design also balances the inability to fiducialize along the vertical axis against the longer electron drift time in a taller TPC, which requires longer veto windows and higher voltages. Considering possible effects of drift time on SEs (see Sec. IV G), other designs may be motivated by future work.

b. γ-ray vetoes: the TPC is surrounded by two vetoes. These instrumented LAr volumes provide passive buffers and anti-coincidence signals when γ-rays deposit energy in them before or after scattering in the TPC. **PDM buffer veto:** Reflective and wavelength-shifting foils (*e.g.* TPB-coated ESR and acrylic surfaces) surround both PDM arrays and the acrylic vessel, optically decoupling them from the LAr bath while enhancing light collection efficiency. The 10 cm offset between each optical plane and the acrylic vessel serves as a "buffer" veto for γ-rays emitted by the PDMs and associated hardware. This offset allows cm-scale spatial resolution, and larger offsets marginally impact the background rate. Veto scintillation is separated from S1 and S2 in the TPC by pulse-shape and the concentration of light in either PDM plane. **Bath veto:** The 4.5 t UAr in the cryostat is instrumented with PDMs on the cryostat walls and functions as another γ-ray veto. This 28 cm buffer uses the minimal UAr mass needed to veto and shield against γ-rays from the cryostat and render their backgrounds subdominant.

c. Water shielding: the cryostat is in a 8–10 m-diameter water tank that shields against external radiation. If a cosmic-ray veto is needed, the tank can be instrumented to detect Cherenkov light.

III. Detector response model

The detector response model closely follows that in Refs. [27, 36]. For a nuclear recoil (NR) of energy E_R, this model uses the reduced energy ϵ, defined as

$$\epsilon = 0.626 \frac{a_0}{e^2} \frac{E_R}{2Z^{7/3}} \tag{1}$$

with target atomic number Z, Bohr radius a_0, and elementary charge e, giving $a_0/e^2 = 36.81/\text{keV}$.

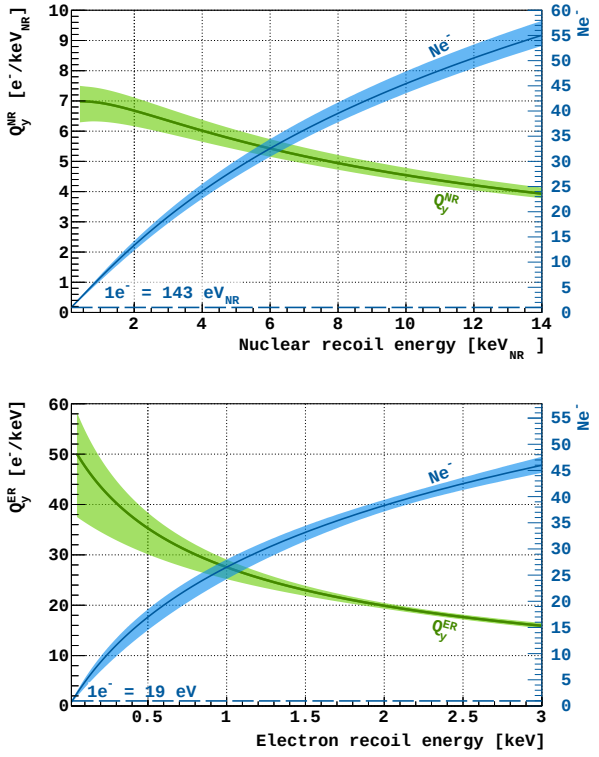

FIG. 2. Ionization yield models assumed in these studies for (top) nuclear recoils and (bottom) electronic recoils. Bands show ±1σ uncertainty from the fit to constraints.

The number of ionization electrons that escape recombination and contribute to S2 is given by

$$N_e^{\text{NR}} = \frac{\mathcal{E}_d^B}{c_\square^{\text{NR}}} \ln \left| 1 + \frac{10^4 f_B c_\square^{\text{NR}}}{\mathcal{E}_d^B} \frac{\epsilon S_e(\epsilon)}{S_e(\epsilon) + S_n(\epsilon)} \right| ; \tag{2}$$

f_B describes the energy partition among ionization and other modes, $c_\square^{\rm NR}$ is a parameter describing the spatial extent of the NR charge distribution, $\mathcal{E}_d$ is the drift field strength in V/cm, B parameterizes the drift field scaling, and S_e and S_n are the electronic and nuclear stopping powers, given in Ref. [37] by

$$\begin{aligned} S_e &= 0.133\frac{Z^{2/3}}{A^{1/2}}\sqrt{\epsilon} \\ S_n &= \frac{\ln\left|1.+1.1383\epsilon_Z\right|}{2\left(\epsilon_Z+0.01321\epsilon_Z^{0.21226}+0.19593\epsilon_Z^{0.5}\right)} \end{aligned} \tag{3}$$

where $\epsilon_Z = 0.94\epsilon$ for argon, accounting for atomic screening effects, and A is the mass number of argon.

For ERs, the number of electrons escaping recombination is described by the Thomas-Imel model as

$$N_e^{\rm ER} = \frac{\mathcal{E}_d^B}{c_\square^{\rm ER}}\ln\left|1+\frac{c_\square^{\rm ER}}{\mathcal{E}_d^B}\rho E_R\right|+1 \tag{4}$$

where the initial recoiling electron has been added to $N_e^{\rm ER}$, and ρ, $c_\square^{\rm ER}$, and B are model parameters.

TABLE II. (Top) $Q_y^{\rm NR}$ and $Q_y^{\rm ER}$ and (Bottom) optical model parameters. Fixed parameters are shown with their assumed values; fit parameters are shown with their best-fit values to external data and the range over which they were allowed to float in sensitivity projections.

	Charge yield parameters		
	Bounds	Modeled value	Units
$\mathcal{E}_d$	Fixed	200	V/cm
B	Fixed	0.61	—
$c_\square^{\rm NR}$	[0.51, 2.04]	$1.02^{+0.01}_{-0.03}$	$(\text{V/cm})^B$
f_B	[0.35, 1.38]	$0.69^{+0.04}_{-0.05}$	—
$c_\square^{\rm ER}$	[0.55, 2.18]	$1.09^{+0.19}_{-0.20}$	$(\text{V/cm})^B$
ρ	[27, 106]	53^{+12}_{-10}	keV^{-1}
	S2 response parameters		
	Modeled value	Units	
$\epsilon_{\rm ph}$	0.27	PE/photon	
$Y_{\rm ph}^{\rm S2}$	280	photon/e^-	
g_2	75	PE/e^-	
σ_{xy}	2.8	cm	
$v_{\rm drift}$	0.93	mm/µs	

The charge yield is defined as $Q_y^{\rm NR} = N_e^{\rm NR}/E_R$ and $Q_y^{\rm ER} = (N_e^{\rm ER}-1)/E_R$. Nuisance parameters f_B, $c_\square^{\rm ER}$, $c_\square^{\rm NR}$, and ρ are constrained by $Q_y^{\rm NR}$ and $Q_y^{\rm ER}$ measurements reported by ARIS [38] and SCENE [39], as well as *in situ* measurements reported by DarkSide-50 [15, 27]. This treatment follows that in Ref. [27], constrained to energies below 3 $\text{keV}_{\rm ee}$. Since the Thomas-Imel model is valid for ERs in this full range, the extended model developed in Ref. [27] is not needed here. Furthermore, B is fixed to the central value reported by SCENE of $B = 0.61$. Studies varying $\mathcal{E}_d$ between 200–1000 V/cm show that its effects on $Q_y^{\rm NR,ER}$ do not impact the projected sensitivity due to the low recombination rate at these energies. As a result, $\mathcal{E}_d$ can be optimized based on its influence on other parameters like $v_{\rm drift}$; such studies are left to future work. Fig. 2 shows the models that best fit these constraints; Table II gives fixed and fit parameters.

Quenching and recombination $N_e^{\rm NR}$ fluctuations are modeled with a binomial function; uncertainties in this treatment are explored by projections with no quenching fluctuations. Binomial $N_e^{\rm ER}$ fluctuations are suppressed by a Fano-like factor F, as in `NEST` [40], constrained by fits to ^{37}Ar peaks in Ref. [27]. Ref. [27] assumes Gaussian fluctuations with variance FN_{e^-}, valid for $N_{e^-}>10\,e^-$. Lacking lower-energy ER calibration, assumptions are needed to extrapolate below $10\,e^-$. A binomial model reflects variations of energy dissipation via ionization and other modes, while a Gaussian model may describe variations in energy transferred to ionization electrons. Both models fit DarkSide-50's ^{37}Ar peaks. Due to the strong $1\,e^-$ resolution assumed for DarkSide-LowMass, the Gaussian model produces larger fluctuations at low N_{e^-}, giving up to $10\times$ stronger constraints on DM scattering cross sections; DarkSide-50's resolution was dominated by spatial g_2 variations, where g_2 is the S2 gain factor, so these models marginally impact its analysis. Binomial fluctuations in $N_e^{\rm ER}$ suppressed by F are conservatively assumed in the present studies. The number of detected photoelectrons (PE) is drawn from a Poisson distribution with mean $g_2 \times N_e^{\rm NR,ER}$.

A. Optical simulations

Optical simulations were performed with `G4DS` [41], based on `Geant4-10.0` [42]. SiPMs are assumed to be similar to those in Refs. [29, 43, 44], with peak photon detection efficiency (PDE) of 40 %. Lower PDE and optical coverage can be compensated with a stronger electroluminescence field, increasing $Y_{\rm ph}^{\rm S2}$.

Simulations of VUV photons generated uniformly in the gas pocket predict a S2 light collection efficiency of $\epsilon_{\rm ph} = 0.27$ PE/photon with both PDM arrays. Electroluminescence simulations based on Refs. [45, 46] predict a photon yield of $Y_{\rm ph}^{\rm S2} = 280$ photon/e^-. These values give $g_2 = \epsilon_{\rm ph} \times Y_{\rm ph}^{\rm S2} = 75$ PE/e^-, tuned for high $1\,e^-$ detection efficiency and resolution, based on DarkSide-50. By varying the gas pocket thickness and electroluminescence field, g_2 can be varied as needed. These values are summarized in Table II.

To estimate the horizontal position resolution, $\leq$0.3 keV electrons are simulated uniformly in the LAr. S2 photons are generated in the gas pocket for

each extracted electron, offset by $t_{\rm drift}$, the time required to drift electrons from the interaction vertex to the gas pocket. The S2 pulse shape is described in Ref. [47]. Photons that reach the PDMs are registered as PE with probability governed by the PDE.

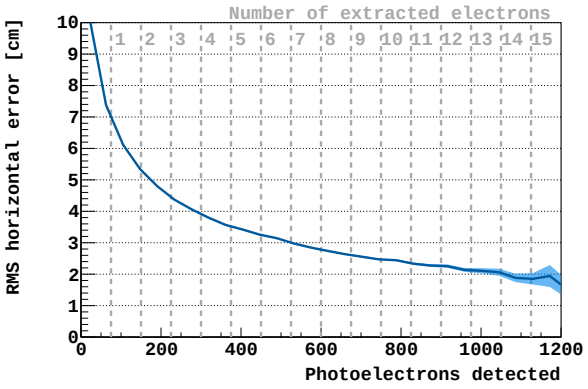

FIG. 3. Horizontal position resolution σ_{xy} as a function of signal size. Between 1–15 e^-, σ_{xy} is between 2–7 cm. The dark line shows the median σ_{xy}, and the lighter band is the 1σ confidence belt from simulation statistics.

The position of a signal in the horizontal plane is estimated using the barycenter method, calculated as the PE-weighted average PDM location and corrected for the expected radial bias near the walls. More sophisticated algorithms can achieve better resolution, as demonstrated in DarkSide-50 [48].

The resolution σ_{xy} is defined as the root mean square (RMS) distance between the reconstructed and true positions. Fig. 3 shows σ_{xy} as a function of S2 charge. Overall, σ_{xy} decreases for larger signals, varying from 2–7 cm for $\geq$1 e^- signals. For background simulations, a nominal resolution of $\sigma_{xy} = 2.8$ cm is assumed, though varying its value within this range does not impact the results presented. While more sophisticated algorithms can likely achieve better resolution, varying the size of the PDMs does not have a significant effect.

IV. Background model predictions

At the highest energies relevant for light DM, the primary backgrounds include γ-rays from detector components, β-decays from LAr radioisotopes, cosmogenic activation of detector materials, surface backgrounds, and neutrinos. At the lowest energies, SEs produce the dominant backgrounds.

A. Neutrinos

CEνNS from solar and atmospheric neutrinos and the diffuse supernova neutrino background (DSνB)

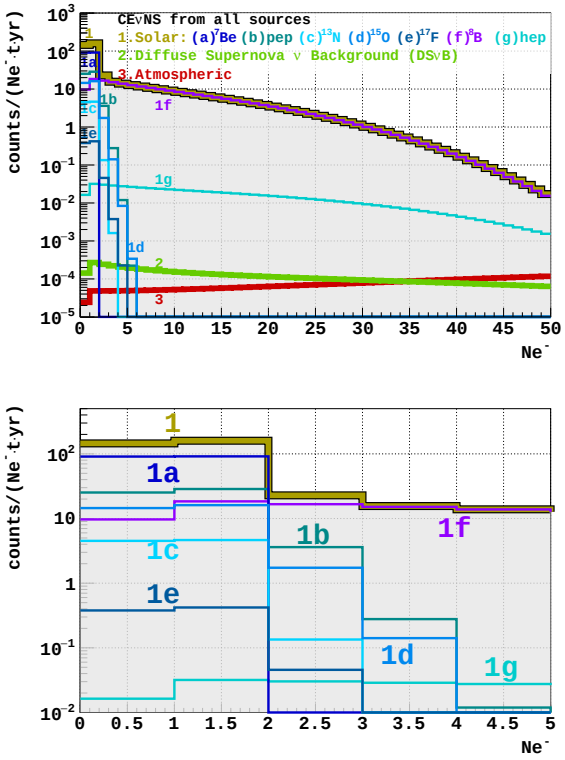

FIG. 4. Coherent elastic neutrino-nucleus scattering background from all sources (*pp* neutrinos not visible), zoomed into *(top)* 0–50 e^- and *(bottom)* 0–5 e^-.

pose a currently-irreducible background. Their fluxes are modeled as in Ref. [49], summarized in Table III, giving (498 ± 12) events/(t yr) between 1–50 e^- (about 0.14–12 keV$_{\rm nr}$ or 0.02–3.4 keV$_{\rm ee}$), dominated by ^{8}B solar neutrinos above 3 e^- and by ^{7}Be, *pep*, and CNO neutrinos below. Neutrino-electron scattering, mostly from *pp* neutrinos, will produce (13.4 ± 0.4) events/(t yr) in the same N_{e^-} range.

TABLE III. Neutrino fluxes assumed in these studies and their associated uncertainties. For solar neutrinos, the high metallicity model was assumed.

	Flux [1/(cm^2 s)]	Uncertainty	Ref.
pp	5.98×10^{10}	0.6 %	[50]
pep	1.44×10^{8}	1 %	[50]
^{7}Be	4.99×10^{9}	3 %	[51]
^{8}B	5.25×10^{6}	4 %	[52]
hep	7.98×10^{3}	30 %	[50]
^{13}N	2.78×10^{8}	15 %	[50]
^{15}O	2.05×10^{8}	17 %	[50]
^{17}F	5.29×10^{6}	20 %	[50]
Atmospheric	10.5	20 %	[53]
DSνB	86	50 %	[54]

Figure 4 shows the CEνNS NR spectra. These irreducible backgrounds lead to the "neutrino fog": the DM-nucleon cross section below which CEνNS

backgrounds impede sensitivity [12, 13]. While solar neutrinos limit the DM search, they enable solar neutrino studies. The fog in Figs. 9 and 11 is given for spectral indices $n = -(d\log\sigma_{\rm SI}/d\log MT)^{-1}$, defining the gradient of the median spin-independent cross section $\sigma_{\rm SI}$ that an experiment can observe at 3σ significance with exposure MT [13].

B. γ-ray backgrounds

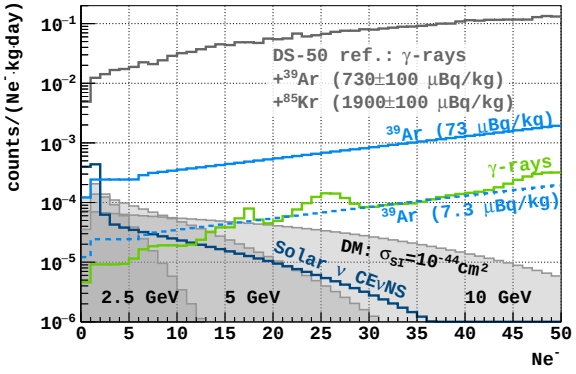

FIG. 5. Backgrounds from γ-rays, ^{39}Ar, and CEνNS, compared to DarkSide-50. DM spectra for are shown at 2.5, 5 and 10 GeV/c^2 masses with spin-independent nucleon-scattering cross section $\sigma_{\rm SI} = 10^{-44}$ cm^2.

Radioisotopes emit γ-rays that scatter in the TPC. Assays from DEAP-3600 [33] and DarkSide are used to estimate the activity of all detector components. Dominant backgrounds include X-rays from the acrylic and γ-rays from the PDMs, including photosensors and their hardware—mostly from ^{40}K and the ^{238}U chain (^{238}U to ^{230}Th).

Radioactive decays in all detector components were simulated using `G4DS` [41]. Energy depositions were recorded in the TPC, bath veto, and PDM buffer veto, and the expected signals were reconstructed using the response model. The electron drift time in the TPC was determined by the drift speed and diffusion in Ref. [47]. Events were rejected by a multiple-scatter cut if at least two S2 signals were separated by >4 µs. The reconstructed position for events in the horizontal plane was determined using the barycenter coordinates smeared by a Gaussian to account for resolution. Varying the smearing within the range in Fig. 3 changes the observed background rate by <10 %. Events outside of the inner 1 t core of the TPC, defined in the horizontal plane, were rejected by a fiducial cut.

Events are rejected if more than 100 keV (50 keV) of energy is deposited in the bath (PDM buffer) veto, within an anti-coincidence window of $t_{\rm drift}^{\rm max} = 1.18$ ms preceding the S2 time. The use of UAr in the vetoes allows thresholds below the ^{39}Ar endpoint; accounting for energy depositions in both vetoes from γ-rays and ^{39}Ar decays, a 3.5–4.0 % dead time is expected, depending on $v_{\rm drift}$ and the ^{39}Ar activity.

Total background rates after selection cuts are shown in Fig. 5, compared to DarkSide-50's best-fit backgrounds and example DM signals. Following veto cuts, the total γ-ray background rate at N_{e^-}<12 e^- is below that from solar neutrinos. No further R&D is needed to improve PDM radiopurity.

1. *Effects of the PDM buffer veto*

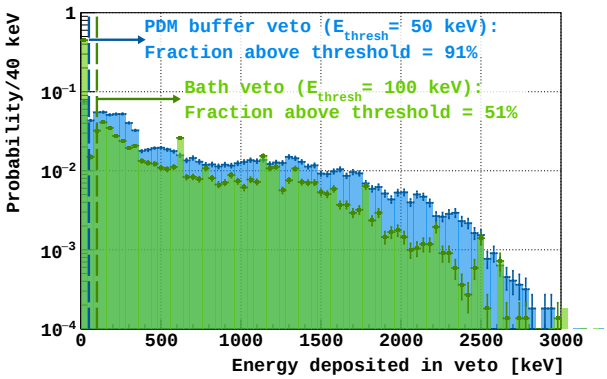

FIG. 6. Energy deposited in (blue) the PDM buffer veto and (green) bath veto for simulated γ-rays from the photoelectronics with <3 keV single-scatters in the TPC fiducial volume, considering both vetoes independently.

The dominant γ-ray background source is the photoelectronics. Since fiducialization along the vertical axis is not possible, low-energy X-rays and γ-rays that preferentially scatter in the first 10 cm of LAr are not mitigated by fiducial cuts. Instead, the PDM buffer shields the TPC from such backgrounds while still allowing those that scatter in it to be tagged.

Figure 6 shows the energy deposited in the vetoes for simulated γ-rays originating in the photoelectronics that produced single-scatters below 3 keV in the fiducial volume. Simulations indicate that the buffer veto can achieve a light yield ≥4 PE/keV, making a 50 keV threshold realistic, and that lower thresholds only marginally improve their efficiency. Since γ-rays can be absorbed in inactive materials after scattering in the TPC, only 51 % are tagged by the bath veto. However, since they must pass through the PDM buffer veto before reaching the TPC, 91 % of the γ-rays that penetrate the buffer and produce a background event are tagged by it.

While the PDM buffer veto and TPC share instrumentation, optical simulations show that pulse shape discrimination efficiently separates scintilla-

tion in the buffers from S2, and the fraction of light concentrated in the top or bottom PDM array allows these signals to be distinguished from S1.

C. β-decay backgrounds

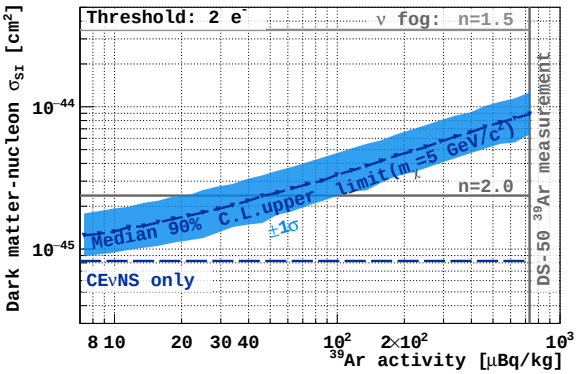

FIG. 7. Median 90% C.L. upper limits and 1σ expectation band on $5\,\mathrm{GeV}/c^2$ DM at varying ^{39}Ar activity.

Two naturally-present β-emitters have been observed in UAr: ^{39}Ar, which DarkSide-50 measured with a specific activity of $(0.73 \pm 0.11)\,\mathrm{mBq/kg}$, and ^{85}Kr, at $(1.9 \pm 0.1)\,\mathrm{mBq/kg}$ [25]. Improvements to the UAr extraction facility [55, 56] are expected to completely remove ^{85}Kr and significantly reduce the ^{39}Ar content relative to DarkSide-50's measurement.

Residual ^{39}Ar can be further suppressed using the Aria facility [26], which will be capable of depleting ^{39}Ar by a factor of 10 at a $(8 \pm 2)\,\mathrm{kg/d}$ throughput.

Starting with an ^{39}Ar activity comparable to DarkSide-50's measurement, the TPC can achieve an activity of 73 µBq/kg with one pass through Aria. With improved UAr extraction and a second pass, this activity may be brought as low as 7.3 µBq/kg.

Potential internal radioisotope activities are summarized in Table IV. The effects of varying the ^{39}Ar activity on the sensitivity to $5\,\mathrm{GeV}/c^2$ DM with a $2\,e^-$ threshold are illustrated in Fig. 7, assuming γ-ray and neutrino backgrounds as discussed above.

TABLE IV. Internal radioisotope activities explored here, with DarkSide-50 measurements for reference [25].

	^{85}Kr	^{39}Ar
	[µBq/kg]	
DarkSide-50	1900 ± 100	730 ± 110
DS-LM	0	7.3–73

D. Cosmogenic backgrounds

Cosmic-rays create backgrounds by activating detector materials in transit and by producing prompt muon-induced signals during operations. FLUKA [57] simulations of muon-induced showers at *Laboratori Nazionali del Gran Sasso* (LNGS) based on Ref. [58] indicate that they pose a negligible background at comparable or greater depths, such as at Boulby Underground Laboratory or SNOLAB. Therefore, these backgrounds are not considered further.

The dominant cosmogenic backgrounds are from UAr activation. Calculations are performed assuming the cosmic-ray neutron flux parameterized in Ref. [59]; correction factors for different altitudes and locations are obtained following Ref. [60]. Production rates and cross sections are taken from measurements and calculations in Refs. [61, 62] and EXFOR [63] whenever available. Otherwise, cross sections are from the JENDL/AN-2005 [64], TENDL [65], or HEAD-2009 [66] libraries or computed from the COSMO [67], YIELDX [68], and ACTIVIA [69] codes.

TABLE V. Expected cosmogenically activated isotopes in UAr, before isotopic purification of argon in Aria.

	^{39}Ar	^{37}Ar	^{3}H
	[µBq/kg]		
Urania→Aria	14.7 ± 1.3	806 ± 73	58 ± 12
Aria (1 mo., surface)	2.57 ± 0.33	294 ± 39	9.0 ± 2.8
Aria→LNGS	0.86 ± 0.11	118 ± 15	3.00 ± 0.95
Aria→N. America	5.73 ± 0.73	483 ± 64	20.0 ± 6.3

Table V shows ^{39}Ar, ^{37}Ar, and ^{3}H yields for trips from the UAr extraction site at Urania (Colorado) to Aria (Sardinia), from Aria to LNGS or North America, and per month outside the underground column at Aria. Atmospheric argon has (40.4 ± 5.0) µBq/kg of ^{42}Ar [70], expected to be orders of magnitude lower in UAr. At sea level, it is activated by successive neutron captures on ^{40}Ar and ^{41}Ar and by $^{40}\mathrm{Ar}(\alpha, 2p)^{42}\mathrm{Ar}$ (14 MeV threshold), at a rate $10^6\times$ lower than ^{39}Ar [71]. Other isotopes have short half-lives or will be removed by purification.

At Aria, (2.57 ± 0.33) µBq/kg/month of ^{39}Ar will be activated in UAr stored above ground during distillation. For long campaigns, these effects can be mitigated by storing UAr underground. If DarkSide-LowMass runs at LNGS or a lab comparably far from Aria, (0.86 ± 0.11) µBq/kg of ^{39}Ar will be activated in transit. At North America, the yield will be (5.73 ± 0.73) µBq/kg. Activated ^{3}H is separated from argon with SAES Getters [72] and will be removed *in situ* while the UAr recirculates; ^{37}Ar will decay away with a 35 day half-life. Hence, neither isotope was included in sensitivity projections.

E. Neutrons

Radiogenic neutrons are produced by (α,n) reactions from trace ^{238}U, ^{235}U, and ^{232}Th in detec-

tor materials. Relevant materials have (α,n) yields around 10^{-6}–10^{-5} [73]. Such neutron backgrounds are therefore expected to be subdominant to those from γ-rays from the same isotopes. These backgrounds are, therefore, not included in this study.

F. Surface backgrounds

The TPC's inner surface area is 5.7 m^2. During construction, ^{222}Rn progeny will deposit on surfaces exposed to air [74], accumulating as ^{210}Pb [75]. Due to its 22.3 yr half life, its activity will be suppressed by a factor of 2132 relative to the deposited ^{222}Rn progeny; by cleaning surfaces [76] and assembling the TPC in a radon-scrubbed clean room [77], ^{210}Pb surface β and X-ray activity can be reduced. Since fiducialization is only in the horizontal plane, cathode cleanliness is particularly important.

While operating, ^{222}Rn can emanate from materials and plate-out on walls, causing surface backgrounds from its decay chain, up to ^{214}Po. These isotopes are efficiently removed from LAr with charcoal radon-traps [33, 78] or molecular sieves [79]; LAr's cold temperature reduces the radon outgassing [80].

TABLE VI. Threshold surface activities of ^{222}Rn and ^{210}Pb decay chains needed to contribute <10 % of the γ-ray background rate, $\mathcal{A}_{\rm thr}$, compared with the activities reported by DarkSide-50 [25] and DEAP-3600 [24].

Isotope	$\mathcal{A}_{\rm thr}$	DarkSide-50	DEAP-3600
	[mBq/m^2]		
^{222}Rn	6.01 ± 0.25	—	$<5 \times 10^{-3}$
^{210}Pb	2.21 ± 0.05	2.51 ± 0.01	0.26 ± 0.02

Surface backgrounds can be controlled through radon-scrubbing and mitigation procedures. To determine the activity at which they pose a significant background contribution, the ^{222}Rn and ^{210}Pb decay chains were simulated within the inner 50 µm of the TPC walls, following the same procedure as for γ-rays. Upper limits on their activity were then set such that surface backgrounds contribute <10 % of the γ-ray background rate from TPC components.

Results from these simulations are given in Table VI, compared with surface background rates reported by DarkSide-50 [25] and DEAP-3600 [24]. Surface activities obtained by other LAr DM detectors are comparable to or below these limits. As a result, these backgrounds are not further considered.

G. Spurious electron backgrounds

In DarkSide-50, SEs dominate signals below 4 e^-. Leading hypotheses stipulate that they are produced by photo- and electrochemical interactions, rather than by particles scattering in LAr. SEs are classified into two categories based on their temporal correlation with preceding progenitor events. Those within the maximum drift time of electrons in the TPC, $t_{\rm drift}^{\rm max}$, are described in Ref. [28] and are consistent with photoionization of detector materials. By requiring the time between pulses to be longer than $t_{\rm drift}^{\rm max}$, such backgrounds are removed from analysis.

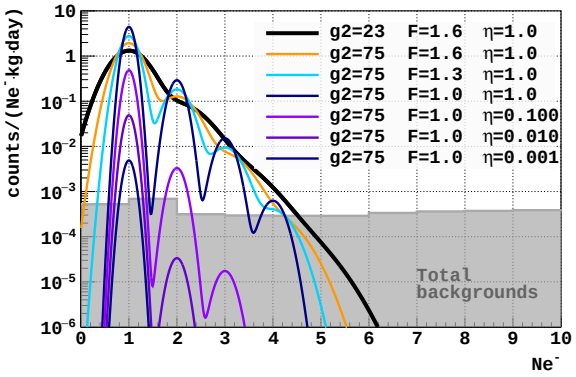

FIG. 8. SE spectra scaled from DarkSide-50 using Eq. (5) and Eq. (6), for different electron amplification factors g_2, excess noise factor F, and impurity scaling factors η. Backgrounds from other sources are shown for comparison, assuming a 73 µBq/kg ^{39}Ar activity.

At longer delays, a large fraction of SEs follow preceding S2 signals by a ∼5 ms or ∼50 ms exponential lifetime, with matching horizontal positions; a third component extends to several seconds. The SE rate is correlated with the total event rate and progenitors' drift time, and it increases when the getter used for purification is turned off. While a full understanding of SEs requires further investigation, their properties are consistent with impurities capturing and later releasing drifting electrons. Similar mechanisms have been proposed in xenon [81]. In this case, SEs may be reduced with purer LAr, achievable with Aria and improved *in situ* purification. The cold temperature of the LAr bath may also slow impurity diffusion. Studies of electron attachment in LAr indicate that attachment coefficients can be decreased by tuning the drift field strength [82, 83].

With improved event reconstruction, it may also be possible to mitigate SEs through their correlations with progenitors. After correcting for pulse-finding efficiency, the N_{e^-} distribution of SEs in DarkSide-50 is consistent with a Poisson distribution, implying that SEs above 1 e^- may be due to pileup. This explanation is supported by a pulse shape analysis. Therefore, improved SE reconstruction with higher N_{e^-} resolution may allow pileup to be tagged, suppressing backgrounds above 1 e^-.

Due to their uncertainties, a full *ex situ* SE model is not possible. For most present studies, the N_{e^-} value below which they dominate sets an analysis

threshold, with $2\,e^-$ and $4\,e^-$ thresholds considered.

To explore effects of SEs beyond their imposition of an N_{e^-} threshold, studies will assume a model motivated by DarkSide-50. This model assumes SEs are produced following an ionization event where some electrons are trapped and later released. If $k{+}1$ electrons are released close in time ($k = 0$ corresponding to $1\,e^-$), they may appear as a single S2 pulse, leading to an SE with $>1\,e^-$. Resolution smearing, determined by g_2 and its spatial variance, may cause them to be reconstructed with $n \neq k$ electrons. The rate of SEs with n electrons is modeled as

$$\begin{aligned} \mathrm{SE}(n) =& R\sum_{k=0}\mathrm{P}(k;p)G\left(n;k+1,F\sqrt{\frac{k+1}{g_2}}\right) \\ \mathrm{P}(k;p) =& \frac{1}{k!}\left(\frac{p^k}{k+1}-\frac{p^{k+1}}{k+2}\right), \end{aligned} \tag{5}$$

where R is the rate per unit mass; G estimates the Gaussian probability of reconstructing n electrons, given mean k and standard deviation $F\sqrt{k/g_2}$; and F accounts for excess noise beyond PE counting statistics (*e.g.* from spatial g_2 variations).

$\mathrm{P}(k;p)$ is the probability of k electrons reconstructing in one S2, given a pileup probability p. It accounts for the probability of two or more electrons appearing in the same S2 window, which decreases with the exponential decay time of captured electrons. This model is fit to DarkSide-50 data and scaled using

$$\begin{aligned} R \propto& R_{\mathrm{trig}} \times L^{\mathrm{max}}_{\mathrm{drift}} \times \eta/M_{\mathrm{fid.}} \\ p \propto& L^{\mathrm{max}}_{\mathrm{drift}} \times \eta \end{aligned} \tag{6}$$

where R_{trig} is the trigger rate, $L^{\mathrm{max}}_{\mathrm{drift}}$ is the maximum drift length, M_{fid} is the fiducial mass, and η scales the impurity concentration relative to DarkSide-50.

SE spectra for different parameter values are shown in Fig. 8. The bold black curve shows a simple extrapolation from DarkSide-50's best-fit F and g_2. Increasing g_2 and lowering F can decrease the tails of the SE distribution. Decreasing the impurity concentration by 10–100 $\times$ further suppresses SEs, enabling thresholds as low as $2\,e^-$. Additional suppression of SEs with $N_{e^-} > 1$ may be achievable with analysis cuts narrowing the pileup window, thereby decreasing p. Such cuts will be strengthened by improved reconstruction with higher g_2 and lower F.

V. Sensitivity projections

DarkSide-LowMass's sensitivity is projected for various scenarios using the profile likelihood ratio test statistic (as defined in Eq. 11 of Ref. [91]) with the CL_s technique (following Ref. [92]) and a Neymann construction to predict median 90% C.L. upper limits for a 1 t yr exposure. These tests used the asymptotic approach with an Asimov dataset, as described in Ref. [91] after confirming that it yields indistinguishable results from generating test statistic distributions with a toy Monte Carlo. Calculations follow the recommendations in Ref. [49], including the Standard Halo Model described in Refs. [93–98].

Figure 7 and the top right of Fig. 9 show how lower background rates improve sensitivity at all masses. Conservative ^{39}Ar and SE background reductions enable exclusion sensitivity into the neutrino fog in a 1 t yr exposure. Realistic scenarios with more SE and ^{39}Ar reduction extend this sensitivity down to $1\,\mathrm{GeV}/c^2$. With 7.3 µBq/kg of ^{39}Ar, doubling the γ-ray background rate weakens limits by $<10\,\%$ ($<20\,\%$) below $5\,\mathrm{GeV}/c^2$ ($10\,\mathrm{GeV}/c^2$).

Figure 10 shows rapid sensitivity growth going from 0.1 to 1 t yr exposure and modest gains extending to 2 t yr. Longer exposures marginally improve sensitivity, as neutrino backgrounds limit sensitivity. These trends strengthen at lower ^{39}Ar activity.

The top of Fig. 11 shows that DarkSide-LowMass can reach competitive sensitivity in a 1 t yr exposure.

A. Improvements with the Migdal effect

Inelastic atomic effects may cause some scattering DM to transfer additional energy to an electron in the target atom, adding an electronic recoil and an X-ray/Auger cascade to the nuclear recoil. This so-called "Migdal effect" allows light DM to make higher-energy signals than is possible for a pure nuclear recoil [99]. Given the pure nuclear recoil rate dR/dE_{NR}, the inelastic rate for producing nuclear and electronic recoil energies E_{NR} and E_{ER} is

$$\frac{d^2R}{dE_{\mathrm{nr}}dE_{\mathrm{ER}}} = \frac{dR}{dE_{\mathrm{NR}}}\frac{1}{2\pi}\sum_{n,\ell}\frac{dp^c_{q_e}(n\ell\rightarrow E_{\mathrm{ER}})}{dE_{\mathrm{ER}}} \tag{7}$$

where $p^c_{q_e}(n\ell\rightarrow E_{\mathrm{ER}})$ is the probability of an electron with mass m_e in the $(n\ell)$ shell being ejected with momentum $q_e = \mathrm{m}_e\sqrt{2E_{\mathrm{NR}}/\mathrm{m}_N}$ in the nuclear rest frame, with mass m_N. The total deposited energy is $E_{\mathrm{NR}}+E_{\mathrm{ER}}+E_{n\ell}$, where $E_{n\ell}$ ($E_{1s} = 3.2\,\mathrm{keV}$, $E_{2s} = 0.3\,\mathrm{keV}$, and $E_{2p} = 0.24\,\mathrm{eV}$) is the binding energy of shell $(n\ell)$. Signals are modeled as in Ref. [21], summing N_e^{NR} from E_{NR} with N_e^{ER} from $E_{\mathrm{ER}} + E_{n\ell}$. This approach is conservative, given the non-linearity of Q_y^{ER}. Values of $p^c_{q_e}$ for isolated atoms are used for all three shells from Ref. [99]. The reduced binding energy and the band structure of the valence shell in LAr are not accounted for, rendering this treatment conservative [100].

Significant sensitivity to DM masses as low as $30\,\mathrm{MeV}/c^2$ can be achieved by exploiting this effect,

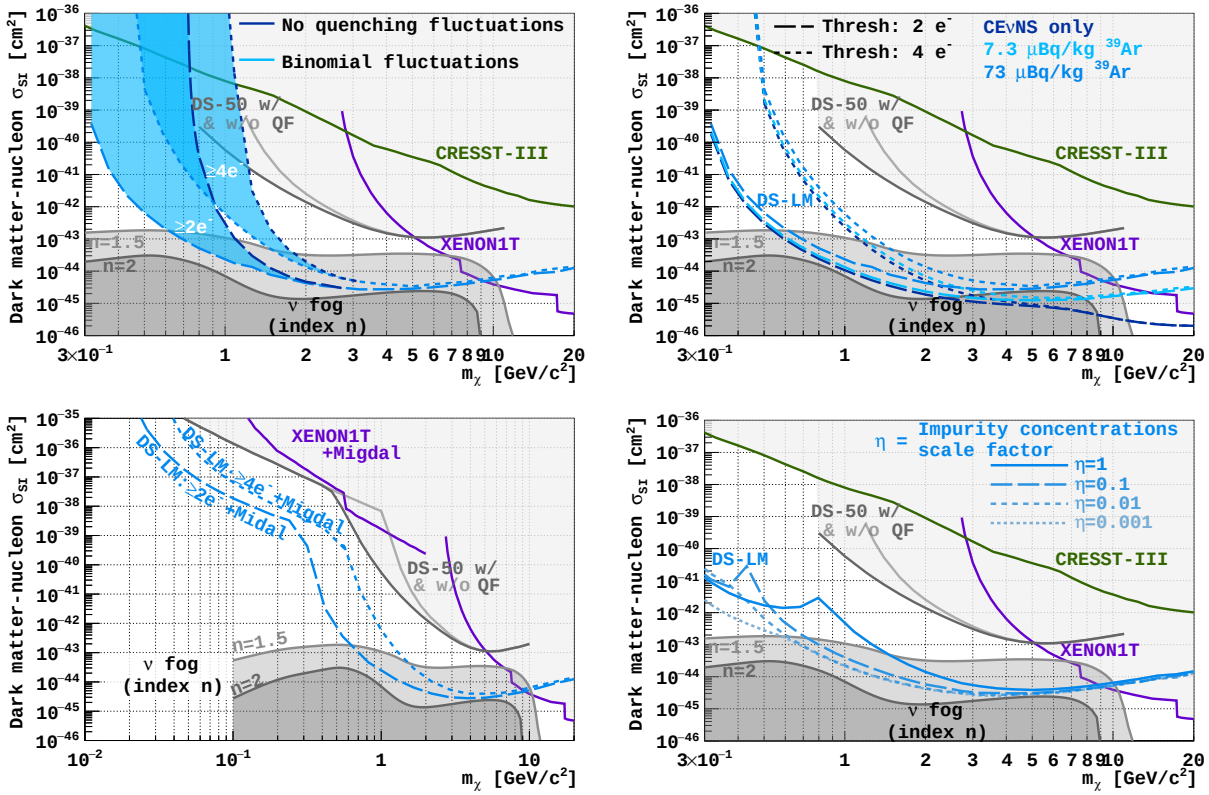

FIG. 9. Projected 90% C.L. upper limits on the spin-independent DM-nucleon scattering cross section for 1 t yr exposure: *(Top, left)* with and without binomial quenching fluctuations. *(Top, right)* with varying thresholds and background rates. *(Bottom, left)* including the Migdal effect. *(Bottom, right)* attempting to model and fit SE backgrounds (see Eq. (5)) at varying impurity concentrations relative to DarkSide-50, η. Unless otherwise stated, projections assume binomial quenching fluctuations and an ^{39}Ar activity of 73 μBq/kg. The neutrino fog in LAr with index n representing the resulting impediment to a 3σ DM observation is shown in shades of gray, calculated to m_χ=100 MeV/c^2 [13]. Current limits are shown from CRESST-III [84], DarkSide-50 [20, 21], and XENON1T [16, 85].

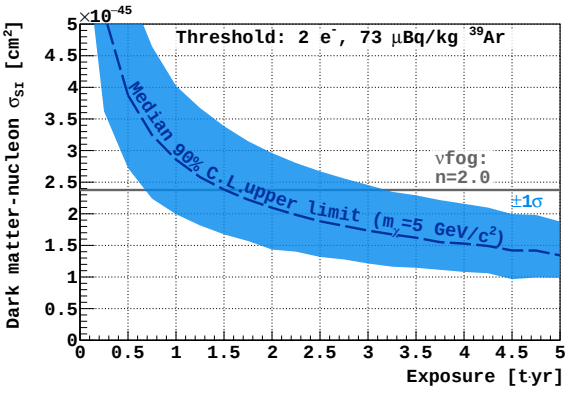

FIG. 10. Median 90% C.L. upper limit and 1σ expectation band for 5 GeV/c^2 DM at varying exposure.

as illustrated in the bottom left of Fig. 9. Other effects may give comparable reach [101].

B. Spurious electron background fits

If R&D enables SE models, they can be included in the profile likelihood ratio calculation, and the analysis threshold can be lowered, recovering sensitivity. The effects of such an analysis are explored by modeling SEs with Eq. (5), with $F = 1$, $g_2 = 75\,\mathrm{PE}/e^-$, and a total event rate of 0.8 Hz, as estimated from simulations. The effects of varying η, the impurity concentration relative to DarkSide-50, are explored.

The results of these fits are shown in the bottom right of Fig. 9. Modeling SEs may extend sensitivity down to 200 MeV/c^2 masses. Kinks in the projected exclusion curves are due to DM spectra that closely match the SE spectrum predicted by a given η.

C. Discovery and evidence sensitivity

The bottom of Fig. 11 shows DarkSide-LowMass's potential for observing evidence of DM at 3σ significance with varying ^{39}Ar concentrations and analysis

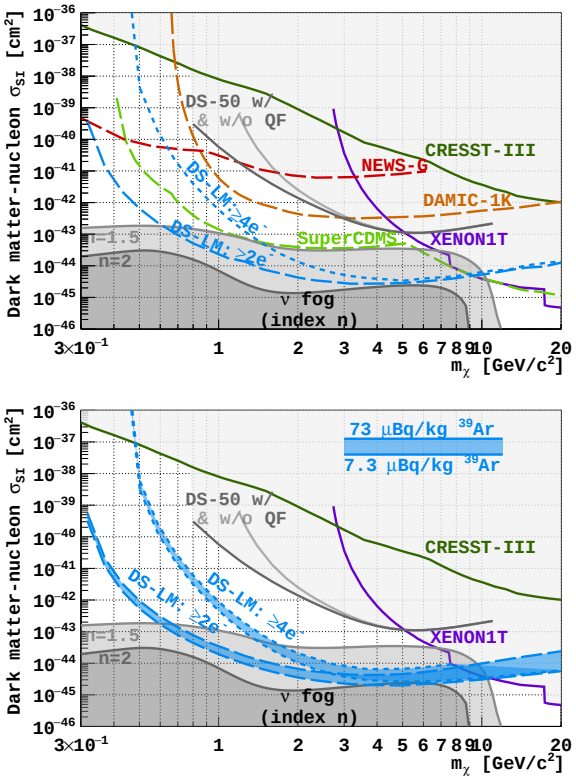

FIG. 11. Projected *(Top)* 90% C.L. exclusion curves for the spin-independent DM-nucleon scattering cross section with 73 µBq/kg of ^{39}Ar, compared to (solid) current and (dashed) projected limits. *(Bottom)* 3σ significance evidence contours with a (dashed) 2 or (dotted) $4\,e^-$ threshold and (thick) 7.3 or (thin) 73 µBq/kg of ^{39}Ar. Binomial quenching fluctuations and 1 t yr exposures are assumed. The neutrino fog in LAr, with n denoting the impediment to a 3σ DM observation, is in gray [13]. Limits from CRESST-III [84], DarkSide-50 [20], and XENON1T [16] are shown, along with DAMIC-1K [86], NEWS-G, and SuperCDMS [87] projections.

thresholds. In 1 t yr, a $4\,e^-$ threshold can reach the $n = 1.5$ neutrino fog above $1.7\,\mathrm{GeV}/c^2$, with significant sensitivity down to $0.5\,\mathrm{GeV}/c^2$. A $2\,e^-$ threshold extends the reach to $0.3\,\mathrm{GeV}/c^2$, with masses above $0.7\,\mathrm{GeV}/c^2$ within the fog. Decreasing the ^{39}Ar activity improves sensitivity at all masses.

TABLE VII. DM masses above which evidence (discovery) contours are within the $n = 1.5$ solar neutrino fog at 3σ (5σ) significance, up to $\sim$10 GeV/c^2.

N_{e^-} threshold [e^-]	^{39}Ar activity [µBq/kg]	3σ [GeV/c^2]	5σ [GeV/c^2]
2	7.3	0.60	0.68
2	73	0.68	0.79
4	7.3	1.42	1.67
4	73	1.71	2.12

An observation rejecting the background-only hypothesis at 3σ significance would constitute evidence for DM, while 5σ amounts to a discovery. Table VII summarizes the masses for which 3σ and 5σ significance is reached within the $n = 1.5$ neutrino fog.

D. Electron-scattering dark matter

DarkSide-LowMass will be sensitive to DM with electronic couplings, via a vector mediator with mass $m_{A'}$. As in Ref. [14], limiting cases of $m_{A'} \gg 1/a_0$ (heavy mediator) and $m_{A'} \ll 1/a_0$ (light mediator) are considered, giving DM form factors $F_{\mathrm{DM}}(q)$ of 1 or $1/(a_0 q)^2$, where a_0 is the Bohr radius and q is the momentum transfer. Fig. 12 shows the projected 90% C.L. exclusion curves and 3σ evidence contours with 1 t yr exposure. Sensitivity to heavy (light) mediators with cross sections down to $10^{-42}\,\mathrm{cm}^2$ ($10^{-38}\,\mathrm{cm}^2$) may be reached at $100\,\mathrm{MeV}/c^2$.

TABLE VIII. DM masses where DM produced by freeze-in ($m_{A'} \ll 1/a_0$) or freeze-out ($m_{A'} \gg 1/a_0$) may be observed at 3σ (evidence) and 5σ (discovery) significance.

N_{e^-} thresh. [e^-]	^{39}Ar activity [µBq/kg]	$m_{A'} \ll 1/a_0$ 3σ [MeV/c^2]	$m_{A'} \ll 1/a_0$ 5σ [MeV/c^2]	$m_{A'} \gg 1/a_0$ 3σ [MeV/c^2]	$m_{A'} \gg 1/a_0$ 5σ [MeV/c^2]
2	7.3	13–1000	15–1000	9–317	9–293
2	73	15–1000	16–1000	9–291	10–270
4	7.3	66–404	—	27–256	27–236
4	73	—	—	28–230	29–192

DM coupled to electrons via a dark photon with $\alpha_D \equiv g_D^2/4\pi$, where g_D is the $U(1)_D$ gauge coupling, can be produced at the relic abundance through the freeze-in mechanism if $m_{A'} \ll 1/a_0$ and the freeze-out mechanism if $m_{A'} \gg 1/a_0$ [90]. Fig. 12 shows the DM-electron scattering cross section $\bar{\sigma}_e$ that gives the relic abundance for DM of mass m_χ with $\alpha_D = 0.5$ and either $m_{A'} \to 0$ or $m_{A'} = 3m_\chi$ for light and heavy mediators, respectively. Away from resonances such as $m_{A'} = 2m_\chi$, these curves vary little with choice of $m_{A'}$ and α_D [90]. Table VIII summarizes m_χ ranges for which DarkSide-LowMass may be able to observe DM with $\bar{\sigma}_e$ predicted by either mechanism with at least 3σ or 5σ significance.

E. Solar neutrino sensitivity

CEνNS from solar neutrinos presents an opportunity to study solar neutrinos through a flavor-universal channel. This reaction was first detected by COHERENT [102, 103], enabling such studies. With a $2\,e^-$ ($4\,e^-$) threshold, an ^{39}Ar activity of 14.6 µBq/kg (7.3 µBq/kg) is required to detect solar neutrinos with 5σ significance in 1 t yr.

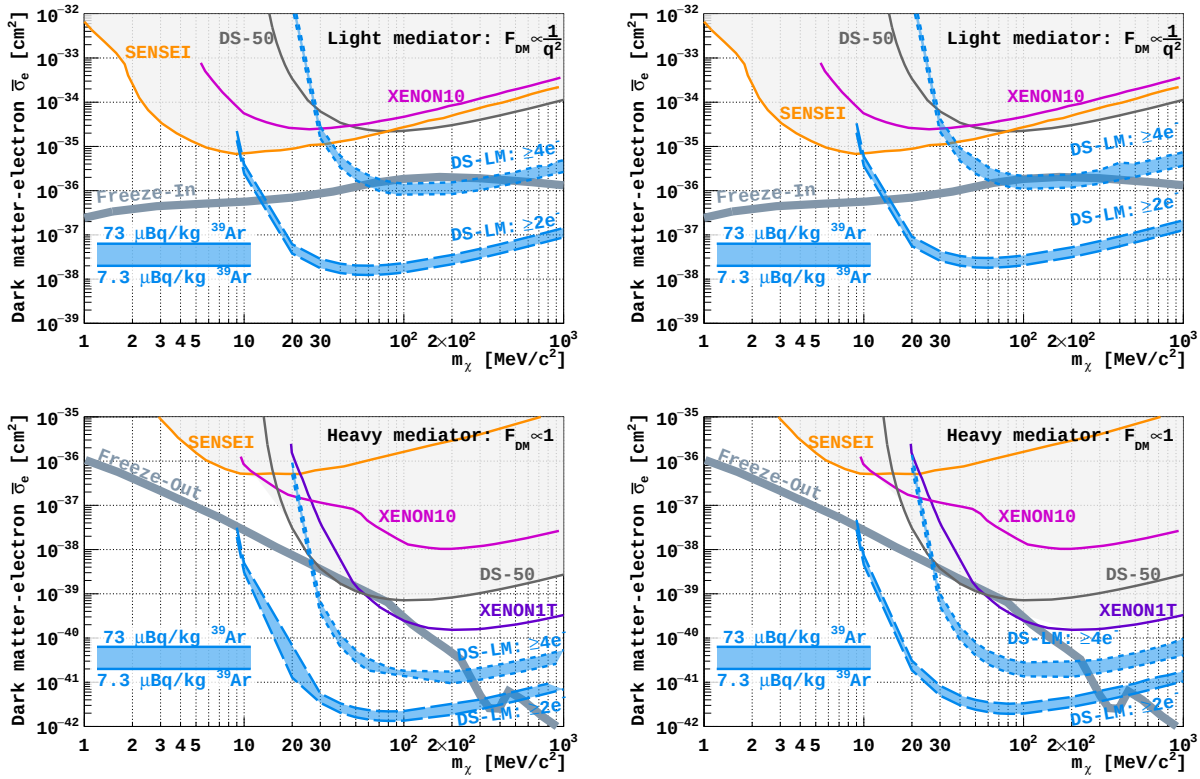

FIG. 12. Projected *(left)* 90% C.L. exclusion curves and *(right)* 3σ significance evidence contours for DM-electron couplings with *(top)* light and *(bottom)* heavy mediators. Bands show 1 t yr contours with 7.3–73 μBq/kg of ^{39}Ar. Limits are shown from DarkSide-50 [22], SENSEI [88], XENON10 [89], and XENON1T [16]. Thick lines show $\bar{\sigma}_e$ giving the relic DM abundance through freeze-in or freeze-out production mechanisms, from Ref. [90].

VI. Ideas for further improvements and upgrades

The small size and relaxed light yield requirements afford DarkSide-LowMass the flexibility to improve its sensitivity through design features, beyond those in the conceptual design discussed in this paper, either as improvements to the baseline design or as future upgrades, pending additional R&D.

DarkSide-50 found that SEs may largely be due to drifting electrons capturing on impurities and later being released. Improvements in the purification system targeting these impurities or modifications that avoid their introduction may therefore reduce SEs, as may techniques for tagging piled-up SEs or fitting them in data. They may also be reduced by shortening the TPC while maintaining the same target mass or by decreasing the total event rate in the fiducial volume. TPB may be one impurity responsible for SEs: it is soluble in LAr [104] and has $\mathcal{O}(1\,\text{ms})$ excited states [105]. Alternatives like the PEN wavelength shifter, VUV-sensitive SiPMs [106, 107], or Xe-doping [108, 109] may therefore reduce SEs.

Doping LAr may also extend sensitivity to lower DM masses [110, 111]: additives with lower ionization energies can increase the yield and lower the energy threshold [112]. At higher concentrations, additives with light nuclei—including hydrogenous photo-ionizing dopants [113]—may offer targets with ideal kinematic coupling to light DM and sensitivity to spin-dependent interactions. Doping LAr in a second phase may be akin to a "beam-on/beam-off" experiment for DM candidates detectable only by the doped target. Since the dominant low-energy backgrounds are SEs, changing the ionization properties of the LAr with dopants may also disambiguate instrumental noise from DM signals. DarkSide-LowMass's small size will afford it the flexibility for such upgrades through a phased approach.

VII. Conclusion

These studies show that a tonne-scale dual-phase LAr TPC with existing technology can reach sensitivity to DM with nuclear couplings in the solar neutrino fog with a 1 t yr exposure. This can be achieved

with a detector similar to DarkSide-50, scaled to a larger target mass with available UAr further suppressed in ^{39}Ar by Aria. In addition to increasing the exposure, the larger mass enables self-shielding, using horizontal fiducialization and the PDM buffer vetoes, to further suppress γ-ray backgrounds.

Present uncertainties in modeling the ionization response of LAr to low-energy nuclear and electronic recoils hinder analyses at lower masses: the top left panel of Fig. 9 illustrates the effects of how ionization yield fluctuations are modeled, while Ref. [27] shows that the choice in nuclear recoil screening function may increase Q_y^{NR} by nearly a factor of two below 10 keV$_{\mathrm{nr}}$, relative to the model by Ziegler *et al.* [37] considered in this work. New measurements below 10 keV, similar to those in Ref. [38, 39], may address these uncertainties and benefit DarkSide-LowMass.

Improved radiopurity, including low-radioactivity SiPMs, and the γ-ray veto system enable a design in which γ-ray backgrounds are subdominant to those from solar neutrinos. The strongest factors for improving sensitivity are further removing ^{39}Ar, with expected gains down to 7.3 µBq/kg, and lowering the energy threshold. DarkSide-LowMass's relatively small target mass allows its UAr to be depleted by Aria in a feasible timescale. Little sensitivity is gained with exposures larger than ∼1 t yr, characteristic of DM searches in the neutrino fog. While these improvements will extend DarkSide-LowMass's sensitivity, especially at lower masses, this fog is already within reach for readily-realizable scenarios. More novel upgrades in a second phase of the experiment can mitigate backgrounds to reach into the neutrino fog for a wider range of DM masses, and they can extend sensitivity to lighter candidates.

VIII. Acknowledgments

The DarkSide Collaboration would like to thank LNGS and its staff for invaluable technical and logistical support. This report is based upon work supported by the U. S. National Science Foundation (NSF) (Grants No. PHY-0919363, No. PHY-1004054, No. PHY-1004072, No. PHY-1242585, No. PHY-1314483, No. PHY- 1314507, associated collaborative grants, No. PHY-1211308, No. PHY-1314501, No. PHY-1455351 and No. PHY-1606912, as well as Major Research Instrumentation Grant No. MRI-1429544), the Italian Istituto Nazionale di Fisica Nucleare (Grants from Italian Ministero dell'Istruzione, Università, e Ricerca Progetto Premiale 2013 and Commissione Scientific Nazionale II), the Natural Sciences and Engineering Research Council of Canada, SNOLAB, and the Arthur B. McDonald Canadian Astroparticle Physics Research Institute. We acknowledge the financial support by LabEx UnivEarthS (ANR-10-LABX-0023 and ANR18-IDEX-0001), the São Paulo Research Foundation (Grant FAPESP-2017/26238-4), Chinese Academy of Sciences (113111KYSB20210030) and National Natural Science Foundation of China (12020101004). The authors were also supported by the Spanish Ministry of Science and Innovation (MICINN) through the grant PID2019-109374GB-I00, the "Atraccion de Talento" grant 2018-T2/TIC-10494, the Polish NCN (Grant No. UMO-2019/33/B/ST2/02884), the Polish Ministry of Science and Higher Education (MNiSW, grant number 6811/IA/SP/2018), the International Research Agenda Programme AstroCeNT (Grant No. MAB/2018/7) funded by the Foundation for Polish Science from the European Regional Development Fund, European Regional Development Fund, the European Union's Horizon 2020 research and innovation program under grant agreement No 952480 (DarkWave), the Science and Technology Facilities Council, part of the United Kingdom Research and Innovation, and The Royal Society (United Kingdom), and IN2P3-COPIN consortium (Grant No. 20-152). I.F.M.A is supported in part by Conselho Nacional de Desenvolvimento Científico e Tecnológico (CNPq). We also wish to acknowledge the support from Pacific Northwest National Laboratory, which is operated by Battelle for the U.S. Department of Energy under Contract No. DE-AC05-76RL01830. This research was supported by the Fermi National Accelerator Laboratory (Fermilab), a U.S. Department of Energy, Office of Science, HEP User Facility. Fermilab is managed by Fermi Research Alliance, LLC (FRA), acting under Contract No. DE-AC02-07CH11359. For the purpose of open access, the authors have applied a Creative Commons Attribution (CC BY) public copyright license to any Author Accepted Manuscript version arising from this submission.

[1] Planck Collaboration, *Planck 2018 results. VI. Cosmological parameters*, Astron. & Astrophys. **641**, A6 (2020).

[2] DarkSide Collaboration, *Results from the first use of low radioactivity argon in a dark matter search*, Phys. Rev. D **93**, 081101 (2016).

[3] DEAP Collaboration, *Constraints on dark matter-nucleon effective couplings in the presence of kinematically distinct halo substructures using the DEAP-3600 detector*, Phys. Rev. D **102**, 082001

(2020).
[4] XENON Collaboration, *Dark Matter Search Results from a One Tonne×Year Exposure of XENON1T*, Phys. Rev. Lett. **121**, 111302 (2018).
[5] LUX Collaboration, *Results from a Search for Dark Matter in the Complete LUX Exposure*, Phys. Rev. Lett. **118**, 021303 (2017).
[6] PandaX Collaboration, *Dark Matter Results from 54-Ton-Day Exposure of PandaX-II Experiment*, Phys. Rev. Lett. **119**, 181302 (2017).
[7] SuperCDMS Collaboration, *Results from the Super Cryogenic Dark Matter Search Experiment at Soudan*, Phys. Rev. Lett. **120**, 061802 (2018).
[8] PICO Collaboration, *Dark Matter Search Results from the* PICO − 60 C_3F_8 *Bubble Chamber*, Phys. Rev. Lett. **118**, 251301 (2017).
[9] D. S. Akerib et al., *Snowmass2021 Cosmic Frontier Dark Matter Direct Detection to the Neutrino Fog*, arXiv:2203.08084, (2022).
[10] DARWIN Collaboration, *DARWIN: Towards the ultimate dark matter detector*, J. Cosmol. Astropart. Phys. **2016**, 017 (2016).
[11] DarkSide Collaboration, *DarkSide-20k: A 20 tonne two-phase LAr TPC for direct dark matter detection at LNGS*, Eur. Phys. J. Plus **133**, 131 (2018).
[12] J. Billard, E. Figueroa-Feliciano, and L. Strigari, *Implication of neutrino backgrounds on the reach of next generation dark matter direct detection experiments*, Phys. Rev. D **89**, 023524 (2014).
[13] C. A. J. O'Hare, *New Definition of the Neutrino Floor for Direct Dark Matter Searches*, Phys. Rev. Lett. **127**, 251802 (2021).
[14] DarkSide Collaboration, *Constraints on Sub-GeV Dark-Matter–Electron Scattering from the DarkSide-50 Experiment*, Phys. Rev. Lett. **121**, 111303 (2018).
[15] DarkSide Collaboration, *Low-Mass Dark Matter Search with the DarkSide-50 Experiment*, Phys. Rev. Lett. **121**, 081307 (2018).
[16] XENON Collaboration, *Light Dark Matter Search with Ionization Signals in XENON1T*, Phys. Rev. Lett. **123**, 251801 (2019).
[17] LUX Collaboration, *Results of a Search for Sub-GeV Dark Matter Using 2013 LUX Data*, Phys. Rev. Lett. **122**, 131301 (2019).
[18] SuperCDMS Collaboration, *Light Dark Matter Search with a High-Resolution Athermal Phonon Detector Operated above Ground*, Phys. Rev. Lett. **127**, 061801 (2021).
[19] PandaX Collaboration, *Dark Matter Search Results from the PandaX-4T Commissioning Run*, Phys. Rev. Lett. **127**, 261802 (2021).
[20] DarkSide-50 Collaboration, *Search for low-mass dark matter WIMPs with 12 ton-day exposure of DarkSide-50*, arXiv:2207.11966 (2022).
[21] DarkSide-50 Collaboration, *Search for dark matter-nucleon interactions via Migdal effect with DarkSide-50*, arXiv:2207.11967 (2022).
[22] DarkSide-50 Collaboration, *Search for dark matter particle interactions with electron final states with DarkSide-50*, arXiv:2207.11968 (2022).
[23] A. Bondar, A. Buzulutskov, A. Grebenuk, D. Pavlyuchenko and Y. Tikhonov, *Electron emission properties of two-phase argon and argon-nitrogen avalanche detectors*, J. Instrum. **4**, P09013 (2009).
[24] DEAP Collaboration, *Search for dark matter with a 231-day exposure of liquid argon using DEAP-3600 at SNOLAB*, Phys. Rev. D **100**, 022004 (2019).
[25] DarkSide Collaboration et al., *DarkSide-50 532-day dark matter search with low-radioactivity argon*, Phys. Rev. D **98**, 102006 (2018).
[26] P. Agnes et al., *Separating* ^{39}Ar *from* ^{40}Ar *by cryogenic distillation with Aria for dark-matter searches*, Eur. Phys. J. C **81**, 359 (2021).
[27] DarkSide Collaboration, *Calibration of the liquid argon ionization response to low energy electronic and nuclear recoils with DarkSide-50*, Phys. Rev. D **104**, 082005 (2021).
[28] DarkSide Collaboration, *A study of events with photoelectric emission in the DarkSide-50 liquid argon Time Projection Chamber*, Astropart. Phys. p. 102704 (2022).
[29] DarkSide Collaboration, *Cryogenic Characterization of FBK RGB-HD SiPMs*, J. Instrum. **12**, P09030 (2017).
[30] R. Essig, G. K. Giovanetti, N. Kurinsky, D. McKinsey, K. Ramanathan, K. Stifter and T.-T. Yu, *Snowmass2021 Cosmic Frontier: The landscape of low-threshold dark matter direct detection in the next decade*, :2203.08297 (2022).
[31] H. O. Back et al., *First Large Scale Production of Low Radioactivity Argon From Underground Sources*, arXiv:1204.6024 (2012).
[32] H. O. Back et al., *A Facility for Low-Radioactivity Underground Argon*, arXiv:2203.09734, (2022).
[33] DEAP Collaboration, *Design and construction of the DEAP-3600 dark matter detector*, Astropart. Phys. **108**, 1 (2019).
[34] M. D'Incecco, C. Galbiati, G. K. Giovanetti, G. Korga, X. Li, A. Mandarano, A. Razeto, D. Sablone and C. Savarese, *Development of a Novel Single-Channel, 24 cm^2, SiPM-Based, Cryogenic Photodetector*, IEEE Trans. Nucl. Sci. **65**, 591 (2018).
[35] M. D'Incecco, C. Galbiati, G. K. Giovanetti, G. Korga, X. Li, A. Mandarano, A. Razeto, D. Sablone and C. Savarese, *Development of a very low-noise cryogenic pre-amplifier for large-area SiPM devices*, IEEE Trans. Nucl. Sci. **65**, 1005 (2018).
[36] F. Bezrukov, F. Kahlhoefer, and M. Lindner, *Interplay between scintillation and ionization in liquid xenon Dark Matter searches*, Astropart. Phys. **35**, 119 (2011).
[37] J. F. Ziegler and J. P. Biersack, presentation at Treatise on Heavy-Ion Science: Volume 6: Astrophysics, Chemistry, and Condensed Matter (1985), edited by D. A. Bromley, pp. 93–129, ISBN 978-1-4615-8103-1.

[38] ARIS Collaboration, *Measurement of the liquid argon energy response to nuclear and electronic recoils*, Phys. Rev. D **97**, 112005 (2018).

[39] SCENE Collaboration, *Measurement of scintillation and ionization yield and scintillation pulse shape from nuclear recoils in liquid argon*, Phys. Rev. D **91**, 092007 (2015).

[40] M. Szydagis et al., *A Review of Basic Energy Reconstruction Techniques in Liquid Xenon and Argon Detectors for Dark Matter and Neutrino Physics Using NEST*, Instrum. **5**, 13 (2021).

[41] P. Agnes et al., *Simulation of argon response and light detection in the DarkSide-50 dual phase TPC*, J. Instrum. **12**, P10015 (2017).

[42] GEANT4 Collaboration, *Geant4—a simulation toolkit*, Nucl. Instrum. Methods Phys. Res. A **506**, 250 (2003).

[43] A. Gola, F. Acerbi, M. Capasso, M. Marcante, A. Mazzi, G. Paternoster, C. Piemonte, V. Regazzoni and N. Zorzi, *NUV-Sensitive Silicon Photomultiplier Technologies Developed at Fondazione Bruno Kessler*, Sensors **19**, 308 (2019).

[44] F. Acerbi et al., *Cryogenic Characterization of FBK HD Near-UV Sensitive SiPMs*, IEEE Trans Electron Devices **64**, 521 (2017).

[45] C. Zhu, Ph.D. thesis, Princeton University (2018), URL https://dataspace.princeton.edu/handle/88435/dsp01qj72p990h.

[46] C. A. B. Oliveira, H. Schindler, R. J. Veenhof, S. Biagi, C. M. B. Monteiro, J. M. F. dos Santos, A. L. Ferreira and J. F. C. A. Veloso, *A simulation toolkit for electroluminescence assessment in rare event experiments*, Phys. Lett. B **703**, 217 (2011).

[47] P. Agnes et al., *Electroluminescence pulse shape and electron diffusion in liquid argon measured in a dual-phase TPC*, Nucl. Instrum. Methods Phys. Res. A **904**, 23 (2018).

[48] J. P. Brodsky, Ph.D. thesis, Princeton University (2015), URL https://dataspace.princeton.edu/handle/88435/dsp01c534fr32w.

[49] D. Baxter et al., *Recommended conventions for reporting results from direct dark matter searches*, Eur. Phys. J. C **81**, 907 (2021).

[50] N. Vinyoles, A. M. Serenelli, F. L. Villante, S. Basu, J. Bergström, M. C. Gonzalez-Garcia, M. Maltoni, C. Peña-Garay and N. Song, *A New Generation of Standard Solar Models*, Astrophys. J. **835**, 202 (2017).

[51] Borexino Collaboration, *Simultaneous precision spectroscopy of pp, ^{7}Be, and pep solar neutrinos with Borexino Phase-II*, Phys. Rev. D **100**, 082004 (2019).

[52] SNO Collaboration, *Combined analysis of all three phases of solar neutrino data from the Sudbury Neutrino Observatory*, Phys. Rev. C **88**, 025501 (2013).

[53] G. Battistoni, A. Ferrari, T. Montaruli, and P. R. Sala, *The atmospheric neutrino fluxes below 100 MeV: the FLUKA results*, Nucl. Phys. B - Proceedings Supplements **145**, 128 (2005).

[54] M. T. Keil, G. G. Raffelt, and H.-T. Janka, *Monte Carlo Study of Supernova Neutrino Spectra Formation*, Astrophys. J. **590**, 971 (2003).

[55] A. Renshaw, *Procuring 50 Tonnes of Underground Argon for DS-20k* (2018), URL https://zenodo.org/record/1239080.

[56] M. Boulay, *DEAP-3600 and Discussion of Multi-Hundred Tonne Argon Program for Dark Matter* (2018), URL https://zenodo.org/record/1239172.

[57] G. Battistoni et al., *Overview of the FLUKA code*, Ann. Nucl. Energy **82**, 10 (2015).

[58] A. Empl, E. Hungerford, R. Jasim, and P. Mosteiro, *A Fluka study of underground cosmogenic neutron production*, J. Cosmol. Astropart. Phys. **2014**, 064 (2014).

[59] M. S. Gordon, P. Goldhagen, K. P. Rodbell, T. H. Zabel, H. H. K. Tang, J. M. Clem and P. Bailey, *Measurement of the flux and energy spectrum of cosmic-ray induced neutrons on the ground*, IEEE Trans. Nucl. Sci. **51**, 3427 (2004).

[60] J. F. Ziegler, *Terrestrial cosmic ray intensities*, IBM J. Res. Dev. **42**, 117 (1998).

[61] R. Saldanha, H. O. Back, R. H. M. Tsang, T. Alexander, S. R. Elliott, S. Ferrara, E. Mace, C. Overman and M. Zalavadia, *Cosmogenic production of ^{39}Ar and ^{37}Ar in argon*, Phys. Rev. C **100**, 024608 (2019).

[62] J. Amare et al., *Cosmogenic production of tritium in dark matter detectors*, Astropart. Phys. **97**, 96 (2018).

[63] V. V. Zerkin and B. Pritychenko, *The experimental nuclear reaction data (EXFOR): Extended computer database and Web retrieval system*, Nucl. Instrum. Methods Phys. Res. A **888**, 31 (2018).

[64] K. Shibata et al., *JENDL-4.0: A New Library for Nuclear Science and Engineering*, J. Nucl. Sci. Technol. **48**, 1 (2011).

[65] A. J. Koning, D. Rochman, J. C. Sublet, N. Dzysiuk, M. Fleming and S. van der Marck, *TENDL: Complete Nuclear Data Library for Innovative Nuclear Science and Technology*, Nucl. Data Sheets **155**, 1 (2019).

[66] Y. A. Korovin, A. A. Natalenko, A. Y. Stankovskiy, S. G. Mashnik and A. Y. Konobeyev, *High energy activation data library (HEAD-2009)*, Nucl. Instrum. Methods Phys. Res. A **624**, 20 (2010).

[67] C. J. Martoff and P. D. Lewin, *COSMO - a program to estimate spallation radioactivity produced in a pure substance by exposure to cosmic radiation on the earth*, Comput. Phys. Commun. **72**, 96 (1992).

[68] R. Silberberg, C. H. Tsao, and A. F. Barghouty, *Updated Partial Cross Sections of Proton-Nucleus Reactions*, Astrophys. J. **501**, 911 (1998).

[69] J. J. Back and Y. A. Ramachers, *ACTIVIA: Calculation of isotope production cross-sections and yields*, Nucl. Instrume. Methods Phys. Res. A **586**, 286 (2008).

[70] DEAP Collaboration, *Electromagnetic Backgrounds and Potassium-42 Activity in the DEAP-3600 Dark Matter Detector*, Phys. Rev. D **100**,

072009 (2019).
[71] C. Zhang and D. M. Mei, *Evaluation of cosmogenic production of 39Ar and 42Ar for rare-event physics using underground argon*, Astropart. Phys. **142**, 102733 (2022).
[72] D. H. Meikrantz, J. D. Baker, G. L. Bourne, R. J. Pawelko, R. A. Anderl, D. G. Tuggle and H. R. Maltrud, *Tritium Process Applications Using SAES Getters for Purification and Collection from Inert Gas Streams*, Fus. Technol. **27**, 14 (1995).
[73] S. Westerdale and P. D. Meyers, *Radiogenic neutron yield calculations for low-background experiments*, Nucl. Instrum. Methods Phys. Res. A **875**, 57 (2017).
[74] V. E. Guiseppe, S. R. Elliott, A. Hime, K. Rielage and S. Westerdale, *A Radon Progeny Deposition Model*, arXiv preprint arXiv:1101.0126, (2010).
[75] D. Nikezić and K. N. Yu, *Exposures to ^{222}Rn and its progeny derived from implanted ^{210}Po activity*, Radiat. Meas. **41**, 101 (2006).
[76] G. Zuzel and M. Wójcik, *Removal of the long-lived ^{222}Rn daughters from copper and stainless steel surfaces*, Nucl. Instrum. Methods Phys. Res. A **676**, 140 (2012).
[77] K. Pelczar, G. Zuzel, M. Wójcik, A. Pocar and A. Ianni, *An online radon monitor for low-background detector assembly facilities*, Eur. Phys. J. C **81**, 86 (2021).
[78] M. K. Harrison, W. H. Lippincott, D. N. McKinsey, and J. A. Nikkel, *Use of activated charcoal for the purification of neon in the CLEAN experiment*, Nucl. Instrum. Methods Phys. Res. A **570**, 556 (2007).
[79] H. Ogawa, K. Abe, M. Matsukura, and H. Mimura, *Development of Low Radioactive Molecular Sieves for Ultra-Low Background Particle Physics Experiment*, J. Instrum. **15**, P01039 (2020).
[80] S. Georgiev, K. Mitev, C. Dutsov, T. Boshkova and I. Dimitrova, *Partition Coefficients and Diffusion Lengths of ^{222}Rn in Some Polymers at Different Temperatures*, Int. J. Environ. Res. Public Health **16**, 4523 (2019).
[81] P. Sorensen and K. Kamdin, *Two distinct components of the delayed single electron noise in liquid xenon emission detectors*, J. Instrum. **13**, P02032 (2018).
[82] G. Bakale, U. Sowada, and W. F. Schmidt, *Effect of an electric field on electron attachment to sulfur hexafluoride, nitrous oxide, and molecular oxygen in liquid argon and xenon*, J. Phys. Chem. **80**, 2556 (1976).
[83] D. W. Swan, *Electron Attachment Processes in Liquid Argon containing Oxygen or Nitrogen Impurity*, Proc. Phys. Soc. **82**, 74 (1963).
[84] CRESST Collaboration, *First results from the CRESST-III low-mass dark matter program*, Phys. Rev. D **100**, 102002 (2019).
[85] XENON Collaboration, *Search for Light Dark Matter Interactions Enhanced by the Migdal effect or Bremsstrahlung in XENON1T*, Phys. Rev. Lett. **123**, 241803 (2019).
[86] DAMIC Collaboration, *Constraints on Light Dark Matter Particles Interacting with Electrons from DAMIC at SNOLAB*, Phys. Rev. Lett. **123**, 181802 (2019).
[87] SuperCDMS Collaboration, *Projected sensitivity of the SuperCDMS SNOLAB experiment*, Phys. Rev. D **95**, 082002 (2017).
[88] SENSEI Collaboration, *SENSEI: Direct-Detection Results on sub-GeV Dark Matter from a New Skipper-CCD*, Phys. Rev. Lett. **125**, 171802 (2020).
[89] R. Essig, T. Volansky, and T.-T. Yu, *New constraints and prospects for sub-GeV dark matter scattering off electrons in xenon*, Phys. Rev. D **96**, 043017 (2017).
[90] R. Essig, M. Fernández-Serra, J. Mardon, A. Soto, T. Volansky and T.-T. Yu, *Direct detection of sub-GeV dark matter with semiconductor targets*, J. High Energ. Phys. **2016**, 46 (2016).
[91] G. Cowan, K. Cranmer, E. Gross, and O. Vitells, *Asymptotic formulae for likelihood-based tests of new physics*, Eur. Phys. J. C **71**, 1554 (2011).
[92] A. L. Read, *Presentation of search results: the CL_s technique*, J. Phys. G **28**, 2693 (2002).
[93] J. D. Lewin and P. F. Smith, *Review of mathematics, numerical factors, and corrections for dark matter experiments based on elastic nuclear recoil*, Astropart. Phys. **6**, 87 (1996).
[94] M. C. Smith et al., *The RAVE survey: Constraining the local Galactic escape speed*, Mon. Notices Royal Astron. Soc. **379**, 755 (2007).
[95] C. McCabe, *The Earth\textquotesingles velocity for direct detection experiments*, J. Cosmol. Astropart. Phys. **2014**, 027 (2014).
[96] R. Schönrich, J. Binney, and W. Dehnen, *Local kinematics and the local standard of rest*, Mon. Notices Royal Astron. Soc. **403**, 1829 (2010).
[97] J. Bland-Hawthorn and O. Gerhard, *The Galaxy in Context: Structural, Kinematic, and Integrated Properties*, Annu. Rev. Astron. Astrophys. **54**, 529 (2016).
[98] GRAVITY Collaboration, *Improved GRAVITY astrometric accuracy from modeling optical aberrations*, Astron. & Astrophys. **647**, A59 (2021).
[99] M. Ibe, W. Nakano, Y. Shoji, and K. Suzuki, *Migdal Effect in Dark Matter Direct Detection Experiments*, J. High Energ. Phys. **2018**, 194 (2018).
[100] R. Catena, T. Emken, N. A. Spaldin, and W. Tarantino, *Atomic responses to general dark matter-electron interactions*, Phys. Rev. Research **2**, 033195 (2020).
[101] J.-H. Guo, Y.-X. Sun, W. Wang, and K.-Y. Wu, *Can sub-GeV dark matter coherently scatter on the electrons in the Atom?*, arXiv:2112.11810, (2021).
[102] COHERENT Collaboration, *Observation of Coherent Elastic Neutrino-Nucleus Scattering*, Science **357**, 1123 (2017).
[103] COHERENT Collaboration, *First Measurement of Coherent Elastic Neutrino-Nucleus Scattering on Argon*, Phys. Rev. Lett. **126**, 012002 (2021).

[104] J. Asaadi, B. J. P. Jones, A. Tripathi, I. Parmaksiz, H. Sullivan and Z. G. R. Williams, *Emanation and bulk fluorescence in liquid argon from tetraphenyl butadiene wavelength shifting coatings*, J. Instrum. **14**, P02021 (2019).

[105] C. Stanford, S. Westerdale, J. Xu, and F. Calaprice, *Surface background suppression in liquid argon dark matter detectors using a newly discovered time component of tetraphenyl-butadiene scintillation*, Phys. Rev. D **98**, 062002 (2018).

[106] T. Igarashi, M. Tanaka, T. Washimi, and K. Yorita, *Performance of VUV-sensitive MPPC for Liquid Argon Scintillation Light*, Nucl. Instrum. Meth. A **833**, 239 (2016).

[107] T. Pershing et al., *Performance of Hamamatsu VUV4 SiPMs for detecting liquid argon scintillation*, J. Instrum. **17**, P04017 (2022).

[108] C. Galbiati, X. Li, J. Luo, D. R. Marlow, H. Wang and Y. Wang, *Pulse shape study of the fast scintillation light emitted from xenon-doped liquid argon using silicon photomultipliers*, J. Instrum. **16**, P02015 (2021).

[109] C. Vogl, M. Schwarz, X. Stribl, J. Grießing, P. Krause and S. Schönert, *Scintillation and optical properties of xenon-doped liquid argon*, J. Instrum. **17**, C01031 (2022).

[110] J. A. LaVerne, A. Hitachi, J. J. Kolata, and T. Doke, *Scintillation and ionization in allene-doped liquid argon irradiated with* ^{18}O *and* ^{36}Ar *ions of 30 MeV/u*, Phys. Rev. B **54**, 15724 (1996).

[111] S. Kubota, A. Nakamoto, T. Takahashi, S. Konno, T. Hamada, M. Miyajima, A. Hitachi, H. Shibamura and T. Doke, *Ionization yield in xenon-doped liquid argon*, Phys. Lett. A **49**, 393 (1974).

[112] H. Ichinose, T. Doke, A. Hitachi, J. Kikuchi, K. Masuda, H. Matsui, E. Otobe, E. Shibamura and T. Takahashi, *Energy resolution for 1 MeV electrons in liquid argon doped with allene*, Nucl. Instrum. Methods Phys. Res. A **295**, 354 (1990).

[113] D. F. Anderson, *New photosensitive dopants for liquid argon*, Nucl. Instrum. Methods Phys. Res. A **245**, 361 (1986).